

Conditioning of cross-flow instability modes using dielectric barrier discharge plasma actuators

Serpieri, Jacopo; Yadala Venkata, Srikar; Kotsonis, Marios

DOI

[10.1017/jfm.2017.707](https://doi.org/10.1017/jfm.2017.707)

Publication date

2017

Document Version

Accepted author manuscript

Published in

Journal of Fluid Mechanics

Citation (APA)

Serpieri, J., Yadala Venkata, S., & Kotsonis, M. (2017). Conditioning of cross-flow instability modes using dielectric barrier discharge plasma actuators. *Journal of Fluid Mechanics*, 833, 164-205.
<https://doi.org/10.1017/jfm.2017.707>

Important note

To cite this publication, please use the final published version (if applicable).
Please check the document version above.

Copyright

Other than for strictly personal use, it is not permitted to download, forward or distribute the text or part of it, without the consent of the author(s) and/or copyright holder(s), unless the work is under an open content license such as Creative Commons.

Takedown policy

Please contact us and provide details if you believe this document breaches copyrights.
We will remove access to the work immediately and investigate your claim.

Conditioning of cross-flow instability modes using dielectric barrier discharge plasma actuators

Jacopo Serpieri,^{1†} Srikar Yadala Venkata^{1,2} and Marios Kotsonis¹

¹AWEF Department, Section of Aerodynamics

Delft University of Technology, Kluyverweg 1, 2629HS Delft, The Netherlands

²Institut PPRIME, Université de Poitiers (CNRS UPR 3346, ISAE-ENSMA), Boulevard Marie et Pierre Curie, BP 30179, 86962 Futuroscope, France

(Received xx; revised xx; accepted xx)

In the current study, selective forcing of cross-flow instability modes evolving on a 45° swept wing at $Re = 2.17 \cdot 10^6$ is achieved by means of spanwise-modulated plasma actuators, positioned near the leading edge. In the perspective of laminar flow control, the followed methodology holds on the discrete roughness elements/upstream flow deformation (DRE/UFD) approach, thoroughly investigated by e.g. Saric *et al.* (1998); Malik *et al.* (1999) and Wassermann & Kloker (2002). The possibility of using active devices for UFD provides several advantages over passive means, allowing for a wider range of operating Re numbers and pressure distributions. In the present work, customised alternating current dielectric barrier discharge plasma actuators have been designed, manufactured and characterised. The authority of the actuators in forcing monochromatic stationary cross-flow modes at different spanwise wavelengths is assessed by means of infrared thermography. Moreover, quantitative spatio-temporal measurements of the boundary layer velocity field are performed using time-resolved particle image velocimetry. The results reveal distinct steady and unsteady forcing contributions of the plasma actuator on the boundary layer. It is shown that the actuators introduce unsteady fluctuations in the boundary layer, amplifying at frequencies significantly lower than the actuation frequency. In line with the DRE/UFD strategy, forcing a sub-critical stationary mode, with a shorter wavelength compared to the naturally selected mode, results in less amplified primary vortices and related fluctuations, compared to the critical forcing case. The effect of the forcing on the flow stability is further inspected by combining the measured actuators body-force with the numerical solution of the laminar boundary layer and linear stability theory. The simplified methodology yields fast and computationally cheap estimates on the effect of steady forcing (magnitude and direction) on the boundary layer stability.

Key words: boundary layer control, boundary layer stability, instability control

1. Introduction

The present study experimentally investigates the effects of using spanwise-modulated alternating current dielectric barrier discharge (AC-DBD) plasma actuators to condition

† Email address for correspondence: j.serpieri@tudelft.nl

cross-flow instability (CFI) modes. The followed strategy follows the upstream flow deformation (UFD) approach, where sub-critical stationary modes of shorter wavelength with respect to the dominant critical mode have been shown to weaken the critical mode and delay transition (Saric *et al.* 1998; Malik *et al.* 1999; Wassermann & Kloker 2002; Hosseini *et al.* 2013). The aim of this study is to identify the pertinent interaction mechanisms between the plasma forcing and cross-flow instability modes, in view of future efforts towards transition delay.

The following sections provide an overview of the published literature on control of CFI and the background of the present study. Thorough reviews on the topic of CFI can be found in Arnal *et al.* (1998); Bippes (1999) and Saric *et al.* (2003). Some more recent studies (e.g. White & Saric (2005); Bonfigli & Kloker (2007); Serpieri & Kotsonis (2016)) further focus on the secondary cross-flow instability.

1.1. Control of cross-flow instability

The term laminar flow control (LFC) generally describes the deployment of passive and active techniques to maintain laminar flow over aerodynamic bodies by delaying laminar-to-turbulent transition. A review of the techniques developed for this purpose was compiled by Joslin (1998). Regarding the specific case of swept wings flows, the main driver of the transition process is the cross-flow instability (Saric *et al.* 2003). The main contributions towards control of cross-flow instability are summarised in Messing & Kloker (2010). In the following discussion, these are shortly described together with the more recent published efforts.

Saric *et al.* (1998) introduced the idea of inducing sub-critical stationary modes, featuring smaller wavelength compared to the naturally dominant modes, to delay transition in three-dimensional (3-D) boundary layers, based on the observations of Reibert *et al.* (1996). Further investigations by Malik *et al.* (1999); Wassermann & Kloker (2002); Hosseini *et al.* (2013) in theoretical and numerical studies confirmed the reported positive effects, towards delaying transition. This approach, named sub-critical discrete roughness elements (DRE) (Saric *et al.* 1998), leads to enhanced amplification of shorter-wavelength modes by means of roughness elements forcing. The term upstream flow deformation is more generally used when making use of any device capable of inducing monochromatic modes (Wassermann & Kloker 2002). The inception of the sub-critical modes leads to a mean-flow deformation which delays the destabilisation of the critical mode thus postponing the amplification of secondary modes and, therefore, the eventual flow breakdown (Wassermann & Kloker 2002). Following the DRE/UFD concept, several studies have been carried out encompassing wind tunnel and free flight experiments as well as numerical simulations. White & Saric (2000) performed wind tunnel campaigns with pneumatically actuated surface roughness elements. Unfortunately, the device did not perform as wished because of technological issues but enhanced the interest towards active LFC based on the DRE/UFD approach. The flow case of the experiment by Saric *et al.* (1998) was later investigated by Hosseini *et al.* (2013) with direct numerical simulations (DNS). Similar outcomes in terms of transition delay were obtained. The extension of the sub-critical DRE/UFD strategy to supersonic flows was demonstrated with the works of Saric & Reed (2002) and Schuele *et al.* (2013) for swept wings and circular cones at incidence, respectively. Flight experiments have also been performed by Tucker *et al.* (2014) and Saric & Banks (2004) in subsonic and supersonic regimes, respectively.

As mentioned, the sub-critical DRE/UFD concepts hold on the same physical mechanism. However, the UFD strategy considers not only surface roughness for the sub-critical forcing of the primary stationary mode. As a fact, a wide range of devices

have been used to force monochromatic stationary cross-flow instability modes. While not primarily intended for flow control, Deyhle & Bippes (1996) made use of localised surface heating spots in order to trigger monochromatic CFI modes. Schuele *et al.* (2013) employed leading edge surface indentations placed at critical and sub-critical (azimuthal) wavelengths. Transition was enhanced by critical forcing and delayed for the sub-critical case with respect to the smooth cone tip (see Schuele *et al.* (2013), figure 27). An array of AC-DBD plasma actuators was also tested, towards the same goal. This was mounted such that the jets induced by the individual localised discharges, would create a boundary layer perturbation similar to that caused by three-dimensional dimples. Indeed the flow arranged similarly in both experiments for the critical forcing case. Unfortunately, the sub-critical case with plasma actuation, and eventual transition postponement, is not reported. In a recent experimental investigation, Lohse *et al.* (2016) applied localised blowing and suction to condition the cross-flow primary instability. They showed effective conditioning of the primary modes by blowing and suction, with the latter being more robust.

It is evident that the global working mechanisms at the basis of the DRE/UFD strategies are sufficiently assessed, through the previous extensive experimental, numerical and theoretical investigations. However, eventual transition delay, with respect to the unforced flow, has not always been demonstrated effectively (Downs & White 2013). The inherent challenges towards successful demonstration of transition delay using DRE/UFD methods suggest a high sensitivity of the approach to a number of factors. Among others, these factors include background surface roughness and free stream turbulence effects (boundary layer receptivity) and Reynolds numbers and pressure distribution effects (boundary layer stability). The latter parameters are crucial as the DRE/UFD strategy has been shown effective only in case the sub-critical control mode is considerably more amplified, closer to the leading edge, than the dominant mode. These considerations deserve further dedicated investigation towards successful and robust implementations of the DRE/UFD technique for effective and efficient LFC.

Relevant contributions to LFC of three-dimensional boundary layers came in the last decade from the group of Dr Kloker at IAG (Institut für Aerodynamik und Gasdynamik) Stuttgart. Several studies were carried out by means of direct numerical simulations investigating different control devices and strategies. In an application to three-dimensional flows, Messing & Kloker (2010) showed that suction effectively enhances boundary layer stability as it leads to fuller streamwise (along the inviscid streamline) velocity profiles at the wall. They also reported that overwhelming suction can lead to undesired promotion of the laminar-to-turbulent breakdown. Messing & Kloker (2010) also studied the combination of distributed suction and UFD in what they refer to as the 'formative suction' approach. The further benefit of the combined technique is the eventual reduction of the required mass flow rate with positive consequences on the energy cost of the active control device.

Pinpoint suction aiming at directly weakening the amplified cross-flow vortices (CFVs) was approached by Friederich & Kloker (2012) and showed beneficial effects in delaying transition. A similar approach, albeit making use of modelled plasma actuators, was more recently published by Dörr & Kloker (2016). The effects of suction holes/plasma actuators positioning, geometry and operational parameters were carefully inspected in these DNS studies. It was shown that, when the forcing is against the cross-flow, the performance of control is highly sensitive to the relative spanwise position between the stationary CFVs and the suction holes/actuators.

Dörr & Kloker (2015b) studied the effect of sub-critical leading edge forcing by means of localised blowing, spots of moving walls (a simplified plasma actuator model) and

plasma actuators. The first technique shows detrimental effects. Transition was promoted by the boundary layer thickening with related momentum loss of the streamwise velocity component. These results were experimentally corroborated by Lohse *et al.* (2016). The other two devices have instead beneficial effects, with plasma actuators being more effective. In this case, as well as in Dörr & Kloker (2016), the plasma actuators are modelled as a steady two-dimensional body-force whose amplitude is retrieved from the induced velocity field. Nevertheless, it is well known that plasma discharges are characterised by strong oscillatory components, which are evident also in the production of the body-force (Corke *et al.* 2010; Benard & Moreau 2014).

Recognising the aforementioned effect, both Dörr & Kloker (2015*b*) and Dörr & Kloker (2016), studied the effect of unsteady forcing. They confirmed the enhancement of only the unsteady travelling mode corresponding to the specific forced frequency. However, the actuated frequencies were well beyond the frequency band of the secondary instability modes. Therefore, the authors acknowledge that, for higher Reynolds number flows compared to their simulations, forcing at such high frequencies could be technologically unfeasible and introduction of undesired flow fluctuations from the actuator might occur.

Recently, Dörr & Kloker (2017) and Dörr *et al.* (2017) used plasma actuators as UFD devices similarly to the work of Schuele *et al.* (2013) on a yawed supersonic cone. The latter work focused on the effects of free stream modes impinging on the forced boundary layer. The actuators effectively induced the shorter-wavelength control mode with consequent beneficial effects on the flow stability. In all these studies, the forcing direction that maximises the flow stabilization is against the local cross-flow. However, even forcing along the CF causes beneficial mean-flow distortions. Shahriari (2016) also followed this approach and presented successful delay of the transition front when the sub-critical control mode was introduced by ring-like plasma actuators. Also in this study, the AC-DBD plasma actuators were modelled as steady body-force sources.

1.2. Plasma actuators for cross-flow instability control

AC-DBD plasma actuators work on the principle of air ionisation (plasma). Through Coulombian interactions, the plasma formation transfers momentum to the surrounding neutral flow, thus leading to localised flow acceleration. Thorough reviews on the working mechanism of these actuators can be found in Corke *et al.* (2010) and Benard & Moreau (2014). Application of AC-DBD plasma actuators for flow control of two-dimensional boundary layers has been extensively studied (see e.g. Grundmann & Tropea (2008); Kotsonis *et al.* (2013, 2015)). In contrast, usage of these devices in three-dimensional flows, dominated by CFI, is still rather limited (see Chernyshev *et al.* (2013); Schuele *et al.* (2013); Dörr & Kloker (2015*b*, 2016, 2017); Shahriari (2016)).

AC-DBD plasma actuators offer several advantages over competing concepts for active LFC. Most of these stem from the pertinent electrical nature of their operation. They feature a broad dynamic range in forcing frequencies, enabled through the direct manipulation of the driving high-voltage signal. Similarly, the induced forcing effect, and hence the actuators authority, can be adjusted by varying the amplitude of the supplied voltage. Furthermore, they do not require pneumatically or mechanically driven devices thus simplifying their operation and maintenance (recall the effort by White & Saric (2000) in this direction). However, these actuators feature some drawbacks. They require high-voltage amplifiers which are still, for many applications, expensive and cumbersome devices. They introduce considerable electromagnetic interference and their lifetime strongly depends on the chosen dielectric material and in specific on its dielectric, mechanical and thermal resistance. However, the main drawback of plasma actuators is their limited control authority at high Reynolds numbers (Corke *et al.* 2010; Benard

& Moreau 2014). As such, one must use plasma actuators for flow control applications in a 'smart' manner, where low energy forcing is applied to highly receptive flows thus producing a large impact downstream. In this regard, Dörr & Kloker (2015*b*) used plasma actuators to reduce the cross-flow velocity component; Jukes & Choi (2013) as vortex generators; Dörr & Kloker (2016) to weaken the CFVs while Schuele *et al.* (2013); Dörr & Kloker (2017) and the present study as localised flow disturbances to condition the CFI modes.

Regarding the specific application to control of CFI, an important consideration is the extreme sensitivity of this type of flow to the surface roughness at the leading edge (cf. Radeztsky *et al.* (1999); Bippes (1999); Saric *et al.* (2003); Kurz & Kloker (2014)). As such, notwithstanding the chosen flow control strategy, the used actuators should feature extremely low levels of roughness when installed on the model surface. AC-DBD can be manufactured accordingly (Schuele *et al.* 2013; Serpieri *et al.* 2017), making them suitable for the control of these flows. However, the effect of using devices that are inherently unsteady on the boundary layer, deserves further dissection (as suggested by Dörr & Kloker (2017) and Serpieri *et al.* (2017)) given the stationary and travelling nature of CFI. The concerns of using fluctuating forcing devices in a laminar boundary layer derive from the possibility of directly/indirectly (the definition of direct/indirect will be discussed in section 8) triggering travelling waves thus promoting the flow breakdown. Furthermore, the secondary instability of the stationary vortices has an unsteady and convective nature (Malik *et al.* 1999; Wassermann & Kloker 2002). Therefore, also the secondary instability mechanisms can be directly influenced by the unsteady actuation (Serpieri & Kotsonis 2017). Pereira *et al.* (2015) reported a dedicated study on the topic, although their flow case was two-dimensional. The mentioned works on CFI-dominated boundary layers, do not fully address the topic as Schuele *et al.* (2013) do not investigate the unsteady flow field and the studies of Dörr & Kloker (2015*b*, 2017) are either based on steady body-force models or on very high frequency actuations. Moreover, in the DNS set-ups of these two studies, the unsteady background disturbances fostering secondary instability are introduced downstream of the actuators location thus partially limiting their outcomes on this regards. These aspects were discussed by P. C. Dörr & M. J. Kloker with the authors in a private communication and are addressed in the current study.

1.3. Previous work at TU Delft and present study

In a recent study, Serpieri & Kotsonis (2016) followed the traditional approach of Reibert *et al.* (1996) of using micron-sized roughness elements to condition the fundamental mode. The development of the primary and secondary instability modes on a swept wing model at chord Reynolds number of $Re=2.17 \cdot 10^6$ was thoroughly investigated with oil flow visualisation, linear stability theory, hot-wire anemometry (HWA) and tomographic-PIV measurements.

In a following study by the same authors (Serpieri & Kotsonis 2017), a diverse application of AC-DBD plasma actuators, not aiming at LFC, was performed. These were mounted close to the location of stationary vortices saturation and used to condition the secondary instability modes. For the purposes of that study, new techniques were developed by the authors enabling the manufacturing and operation of extremely low roughness plasma actuators. The use of such actuators was instrumental in the present study. Preliminary results of the current study were presented by Serpieri *et al.* (2017).

The present study investigates the possibility of conditioning the natural flow arrangement of a transitional swept wing boundary layer by means of AC-DBD plasma actuators, as the first step towards the UFD approach. While similar in concept to the work of

Schuele *et al.* (2013) on the supersonic yawed cone and of Dörr & Kloker (2017) on the swept flat plate simulations, the present study is, to the authors knowledge, the first experimental demonstration of plasma flow control on a swept wing at flight order of magnitude ($O(10^6)$) Reynolds numbers. The primary objective of this study is, thus, the elucidation of the effects of AC-DBD plasma actuators on the development of CFI transition in view of future efforts towards LFC using plasma actuators. Emphasis is given to the investigation of the actuators steady and unsteady effects on the boundary layer. To this goal, infrared (IR) thermography and time-resolved PIV measurements are presented. Additionally, a simplified model of the effects of steady forcing on the flow stability is proposed. This approach leverages upon numerical solutions of the laminar stationary boundary layer equations combined with experimentally extracted body-force fields and linear stability theory (LST).

The article is organised as follows: the experimental set-ups of the infrared flow visualisation and high-speed PIV experiments are introduced in section 2. Section 3 is dedicated to linear stability theory. The tested flow cases are summarised in § 4. The actuator characterisation is performed by a dedicated experiment presented in § 5. The IR thermography and the PIV results are described in § 6 and § 7, respectively. The simplified model of the forcing steady effect is presented in § 8. The conclusions of this study are in section 9. In appendix, the numerical solution used in sections 3 and 8 is described.

2. Experimental Set-up

The wind tunnel model and related coordinate reference systems are introduced here, followed by the description of the custom-made plasma actuators. Setups of the IR thermography and high-speed PIV experiments are eventually described.

2.1. Wing model, wind tunnel and reference systems

The model used in the current investigation is a 45 degrees swept wing of 1.25m span and 1.27m chord in the free stream direction. The airfoil used is a modified version of the NACA 66018 shape that was named *66018M3J* (more details can be found in Serpieri & Kotsonis (2016)), the wing and the airfoil are presented in figures 1b and 5).

The wind tunnel where the experiments were performed is the closed-loop low-turbulence tunnel (LTT) installed at TU Delft Aerodynamics. The tunnel testing chamber dimensions are: 1.25m \times 1.80m \times 2.6m in height, width and length, respectively. Because of seven anti-turbulence screens and a contraction ratio of 17:1, the flow has very low levels of free stream turbulence. The latter was measured with a single hot-wire sensor to be $Tu/U_\infty = 0.07\%$ at the free stream velocity of $U_\infty = 24\text{m s}^{-1}$ (bandpass filtered between 2Hz and 5000Hz). The Tu/U_∞ value is low enough to observe stationary cross-flow waves (see Bippes (1999)) and indeed this was the case for the test case at $U_\infty = 25.6\text{m s}^{-1}$ and free stream Reynolds number $Re = 2.17 \cdot 10^6$ (see also Serpieri & Kotsonis (2016)). The experiment was performed at incidence of $\alpha = 3^\circ$ and the flow over the wing pressure side was investigated.

In order to be used for studies on the cross-flow instability, the flow has to be representative of a semi-infinite swept wing thus invariant along the leading edge direction (Deyhle & Bippes 1996; Radeztsky *et al.* 1999; Reibert *et al.* 1996). The invariance of the flow along the leading edge direction is assessed by two arrays of 46 pressure taps placed near the two wing ends (300mm from the tunnel walls). At $\alpha = 3^\circ$, the flow shows a high degree of uniformity when checking the pressure distributions of the two arrays (see figure 1a). Furthermore it is worth to notice that, for this flow configuration, the

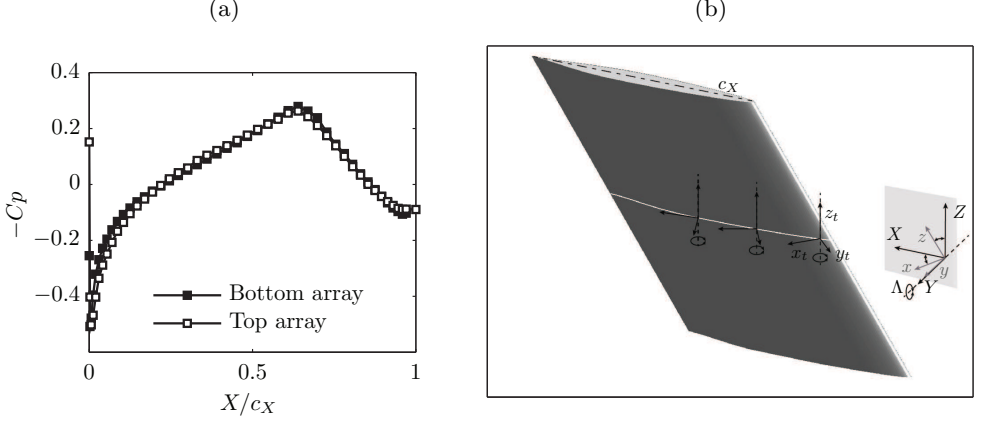


Figure 1: (a) Pressure distribution on the wing pressure side measured by two arrays of 46 pressure taps placed 300mm from the top and bottom wing tips respectively at $\alpha=3^\circ$ and $Re=2.17 \cdot 10^6$. (b) Schematic of the model and definition of the xyz , XYZ and $x_t y_t z_t$ reference systems.

measured pressure minimum point is at $X/c_x=0.63$ thus ensuring a fully stable boundary layer with respect to Tollmien-Schlichting (TS) modes.

Due to the inherent complexity of the geometry and flow topology, several reference systems are introduced. These are presented in figure 1b. Firstly, the unswept coordinate system is defined with the upper case letters XYZ and is positioned such that the X and Y axes lie in a horizontal plane (X being in the chord plane and Y orthogonal to that plane) while the Z is the vertical direction. The velocity components along this coordinate system are indicated with upper case letters UVW . The wing is rotated at incidence angle of $\alpha=3^\circ$ and, as such, the wind-tunnel reference system does not coincide with the unswept wing coordinates. The velocity components along the wind-tunnel reference systems are denoted with upper case letters and the subscript: ∞ .

The swept reference system is such that its x axis is orthogonal to the wing leading edge, the z axis is parallel to the leading edge (both these axes belong to the chord plane) and the y axis coincides with the unswept Y direction. By rotating the XYZ system about the Y axis by $\Lambda=45^\circ$, one goes to the swept xyz system. The velocity components in this system of coordinates are indicated with the lower case letters uvw .

A last coordinate system needs to be introduced as the local tangential system (the definition of tangential is simplified here as it implies only the surface curvature along the X direction). This system is positioned such that its x_t axis is along the surface tangent, the y_t is the wall-normal direction and z_t coincides with the Z axis.

2.2. AC-DBD plasma actuators

As earlier identified, for the needs of this study, actuator-induced roughness is of great importance. To this end, special actuators were designed, built and employed. The actuators were manufactured using a metal deposition technique developed in-house. The technique makes use of computer-controlled spraying of sub-micron conductive silver particles on the dielectric surface. The resulting electrode thickness is of the order of $1\mu\text{m}$. For comparison, traditional hand-made actuators based on adhesive copper

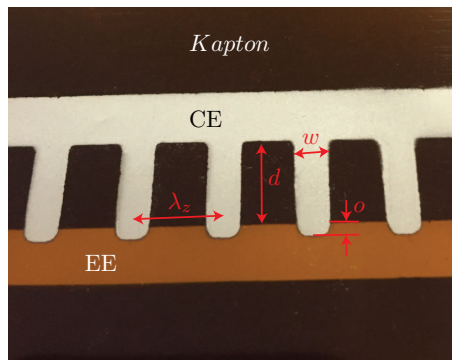


Figure 2: Detail (picture) of a DBD plasma actuator used for selective forcing of monochromatic primary cross-flow instability modes. The *Kapton* sheet, the covered electrode (CE), the exposed electrode (EE), the stems wavelength (λ_z), the width (w), the distance between the electrodes (d) and the overlap (o) are also shown. View of the underside of the actuator, CE on foreground, EE on background.

tape, typically have electrode thickness of $60\mu\text{m}$. The plasma actuators were placed at $x/c=0.025$, close to the primary mode critical station (see the LST analysis of section 3). The plasma actuators were designed towards forcing a single monochromatic primary cross-flow mode. To force the desired mode, the employed actuators feature one straight electrode, which is exposed to the flow and is powered by the high-voltage supply. The grounded electrode is encapsulated below the dielectric barrier and is made of a series of stems spaced equally from each other and oriented along x (see figure 3b). The spacing between the stems defines the spanwise wavelength of the plasma forcing, and as such the spanwise wavelength of the forced CF modes. Three different modes were forced in this study, namely $\lambda_z=9\text{mm}$, which corresponds to critical mode (Serpieri & Kotsonis 2016), and $\lambda_z=7\text{mm}$ and $\lambda_z=12\text{mm}$, corresponding to sub-critical and super-critical modes respectively.

A detail of the DBD plasma actuators used in this study is presented in figure 2. The covered electrode stems are $d=10\text{mm}$ long and $w=3\text{mm}$ wide. They are projected towards the straight electrode overlapping with it by $o=2\text{mm}$, in order to ensure consistent plasma formation. Given the relative large length of these stems, the flow ionisation region corresponds only to the electrode overlapping area thus ensuring the desired spanwise modulation of the forced jet. It is important to note that the exposed electrode was placed downstream such to have the induced jet aligned with $-x$ (see figure 3b).

Kapton polyimide film of $50\mu\text{m}$ thickness was used as dielectric barrier. A second layer of *Kapton* was placed between the actuator and the model surface to better protect the latter. As such, the total thickness of the actuator was measured to be $125\mu\text{m}$. In order to avoid exposure of the incoming flow to a step of such high thickness, the *Kapton* sheet was wrapped around the wing leading edge. This ensured that the only surface perturbation seen by the flow was a two-dimensional backward facing step of $125\mu\text{m}$ at approximately 10% of the model chord. Preliminary investigations, using PIV and infrared thermography, indicated no adverse effects on the transition location by the physical presence of the actuator on the wing.

The actuator was powered using a *Trek 20/20C HS* high-speed high-voltage amplifier. Depending on the case, the actuation signal was sinusoidal with amplitudes (E) between 2kV and 3kV. The scope of this study is to prove the applicability of DBD plasma

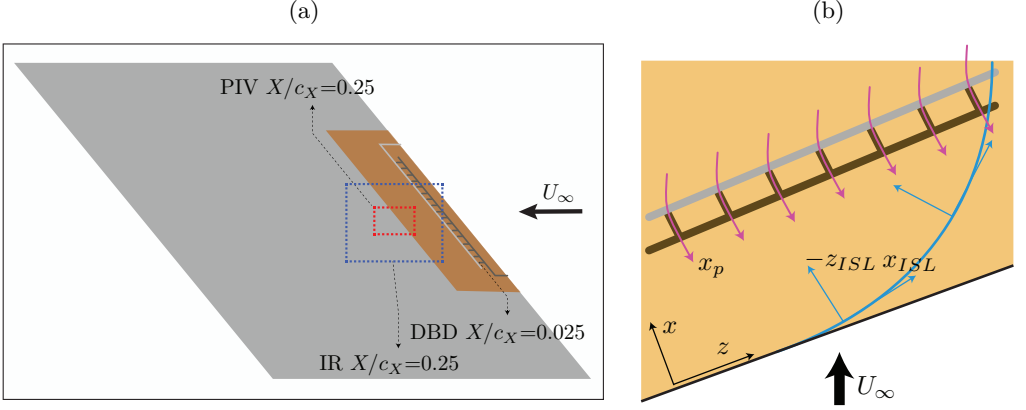


Figure 3: (a) Schematic of the wind-tunnel model with the actuators (*Kapton* sheet in orange, CE in dark grey, EE in light grey). Definition of the FOVs of the IR thermography (blue dashed rectangle) and of the PIV (red dashed rectangle) experiments. (b) Schematic of the plasma actuator. The plasma jets (magenta), the inviscid streamline (cyan) and the related reference system (ISL) are shown together with the swept reference system (xz). The schematics are not to scale.

actuators as control devices to condition the spanwise wavelength of primary cross-flow instability modes. As such, the high-voltage signal frequency (carrier frequency) was chosen considering the development of unsteady instability modes in the boundary layer. Preliminary linear stability theory analysis (presented in section 3) showed that the considered boundary layer is unstable to travelling primary instability modes comprised in the band 0-1kHz. Therefore for the main tested cases, the actuators were operated at 2kHz. To decouple the effects of unsteady forcing from the effects of forcing monochromatic CFI modes, a two-dimensional spanwise-uniform actuator was also considered.

2.3. Infrared thermography

The boundary layer transition evolution was inspected by IR thermography. The model was irradiated by two 1kW halogen lamps placed approximately one metre from the model. The convective heat flux from the wing surface to the flow is a function of the local wall shear. As such, regions of high shear cool more rapidly than respective low shear regions. Differences in wall temperature captured by the thermal camera can therefore be used for visualisation between laminar and turbulent regions (see also Saric *et al.* (2011)). In addition, using highly sensitive, actively cooled thermal imagers, details in the shear distribution of laminar boundary layers, such as the characteristic streaky footprint of CFVs can be retrieved.

The set-up for the IR thermography experiment is presented in the schematic of figure 4a. The camera was mounted at about 1m distance from the model surface and placed outside the wind tunnel, looking through an opportune germanium window. The imaged field of view was $480 \times 360 \text{ mm}^2$ and centred at $X/c_X=0.25$, $Z=0$ (see the schematic of figure 3a, where the IR domain is shown with a dashed rectangle). The IR camera used for the current experiment was a *CEDIP Titanium 530L*, featuring a mercury-cadmium-telluride quantum sensor with $320 \times 256 \text{ px}^2$. The sensor is actively cooled by means of a Stirling cycle to the working temperature of 77K resulting to a noise equivalent temperature difference (NETD) of less than 18mK. The integration time and the operated

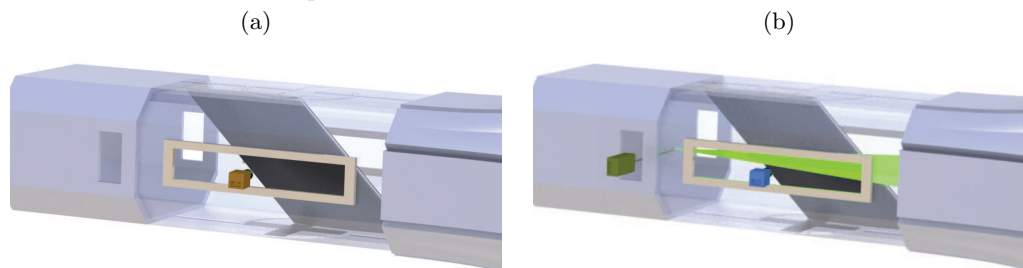


Figure 4: Schematics (not to scale) of the experimental setups. The flow comes from right. The model (in black), the testing chamber (semi-transparent) and the opportune diagnostics windows are shown. (a) IR-thermography experiment with the IR-camera (in brown). (b) high-speed PIV experiment with the PIV camera (in blue), the laser head (in dark green) and the light sheet from downstream (light green).

frame rates were $200\mu\text{s}$ and 100Hz respectively. The camera was equipped with a 25mm focal length germanium lens operated at $f_{\#}=2.0$.

2.4. Particle image velocimetry

Particle image velocimetry was performed towards quantification of the boundary layer velocity field. Planar high-speed PIV was chosen for this experiment. The inspected planes are along the $X - Z$ directions at a distance of 1.5mm from the model surface. The planes are centred with the station $X/c_X=0.25-Z=0$ of the model (see the schematic of figure 3a, where the PIV domain is shown with a dashed rectangle).

The PIV experimental set-up is presented in figure 4b. As shown, the camera was imaging the field of view (FOV) from outside the wind tunnel through available optical windows and was placed at approximately 1m distance from the measured plane. The camera used in this experiment is a *LaVision Imager HS* featuring a sensor of $2016 \times 2016\text{px}^2$ and pixel size of $11\mu\text{m}$ and 12bits of digital resolution. The active image sensor was reduced to $1632 \times 496\text{px}^2$ for the current experiment. The imager was equipped with a *Nikon Nikkor 200mm micro* lens operated at $f_{\#}=5.6$. The resulting magnification factor of the PIV experiment is $M=0.24$. Illumination was provided from downstream as shown in the schematic of figure 4b. A Nd:YAG high-speed *Continuum Mesa PIV* laser (18mJ per pulse) was employed for particle illumination. The light beam was opportunely shaped into a sheet of approximately 1mm thickness. The light sheet was oriented such to be parallel to the model surface for all the imaged domain as shown in figure 5. In the schematic the AC-DBD plasma actuator is also shown. The *Kapton* sheet is in light grey and the electrodes in dark grey. To note that this is the wing cross-section orthogonal to the leading edge direction.

The flow was seeded using *Safex* water glycol injected downstream of the testing chamber. The average particle diameter is $1\mu\text{m}$. Synchronisation of the system was guaranteed by using the *LaVision Davis 8.2* suite and a *LaVision High Speed Controller* unit. Image acquisition, pre-processing and correlation were performed with the same software. Cross-correlation was performed with final interrogation windows of $24 \times 24\text{px}^2$ with relative overlap set to 75%. As such the final vector spacing was approximately 0.27mm in both X and Z . The time interval between the two laser pulses was set to $15\mu\text{s}$ such to give an average particle displacement in the free stream of 15px . The measurement

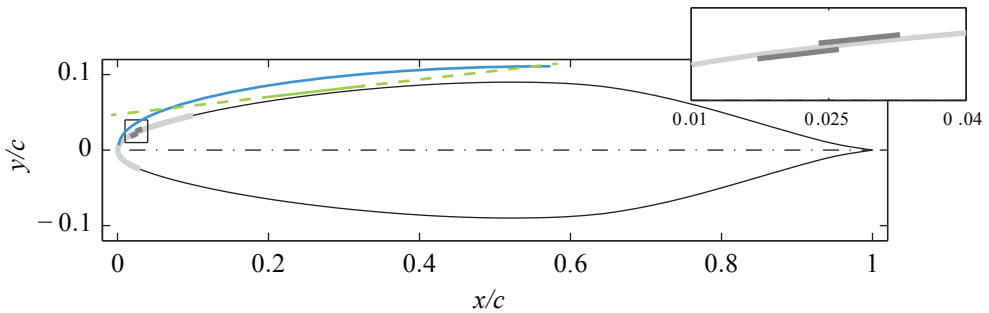


Figure 5: Wing section and schematic (not to scale) of the laser light (light green) and of the boundary layer (cyan). The AC-DBD plasma actuator is also shown: *Kapton* sheet in light grey; electrodes in dark grey. Inset: magnified view of the actuator. The wing section is orthogonal to the leading edge.

frame rate (FR) was 3000Hz and sequences of 6000 image pairs were acquired, for every tested flow case. The resulting measurement time was 2s.

The correlation random error in planar PIV is estimated to be 0.1px (Raffel *et al.* 2007). Therefore the random error, relative to the free stream velocity, is $\varepsilon_{(U,V)} = 0.1/15 = 0.007$. This is also the measurement error for the statistic velocity fluctuations fields ($\{U'_t, V'_t\}_{RMS}$). Here U'_t and V'_t are the time velocity fluctuations (i.e. after subtracting the time average). The uncertainty on the time-averaged velocity fields is retrieved from the flow fluctuations magnitude, estimated to be less than 10% of the free stream velocity, and from the measurement ensemble size (ES): $\varepsilon_{(\bar{U}, \bar{V})} = 0.1/\sqrt{ES}$, where the overbar denotes time averaging. The ensemble size to be considered here does not encompass all the 6000 captured fields. These are correlated in time with respect to the travelling instability modes, which account for most of the fluctuation energy at the measurement location (Serpieri & Kotsonis 2016). The fluctuations related to this instability feature high energy content in the frequency band $100\text{Hz} \leq f \leq 400\text{Hz}$ (Serpieri & Kotsonis 2016). Therefore a conservative time sub-sampling of the measured fields is required in order to formally render them uncorrelated in time. This factor can be estimated as $\text{FR}/\min(f_{(U'_t, V'_t)}) = 3000\text{Hz}/100\text{Hz} = 30$ and is used to estimate the uncorrelated ensemble size as a fraction of the total of the captured samples: $ES_u = ES/30 = 200$. Finally, the uncertainty on the time-averaged velocity fields can be evaluated as $\varepsilon_{(\bar{U}, \bar{V})} = 0.1/\sqrt{ES_u} \approx 0.018$.

2.5. Non-dimensionalisation and normalisation

Several reference systems and different experimental and numerical techniques were used and described in the present study. Part of the results is therefore presented in non-dimensional units. The airfoil chords along the X and x directions are used as reference length scales for the respective coordinate systems. However, some results are presented in dimensional units to ease comparison with dimensional quantities and avoid introduction of elaborated nomenclature. This consideration follows from the actuators employed in this study. These devices can be described by non-dimensional quantities as e.g. the momentum coefficient (see § 5). However, the main dimensional parameters, namely the frequency of the driving AC voltage and the wavelength of the electrodes, are crucial for the description and understanding of the presented analyses. The velocity scale used

in the remainder is the free stream velocity (U_∞). In addition, U_∞^2 is used to non-dimensionalise the velocity power spectra.

When specified, the presented spectra are normalised as shown in equation 2.1 (in agreement with Parseval's theorem),

$$\Phi_\gamma^* \cdot \delta_f = (\Phi_\gamma \cdot \delta_f) \frac{\frac{1}{ES-1} \Sigma_t(\gamma')^2}{\Sigma_f(\Phi_\gamma \cdot \delta_f)} \quad (2.1)$$

where Φ is the power spectral density (PSD), δ_f is the spectra frequency resolution, γ is the spectra variable and ES the temporal ensemble size. The sums are performed with respect to the subscript quantity (i.e. time (t) at the numerator and frequency (f) at the denominator).

3. Stability of the laminar boundary layer

The stability of the laminar boundary layer is investigated by means of numerical solutions of the boundary layer equations and linear stability theory. In two-dimensional boundary layers, LST is a common tool to predict the early (linear) stages of instability growth (Schlichting & Gersten 2000). The extension to three-dimensional flows is straightforward if flow invariance along the leading edge direction is respected (Mack 1984). This hypothesis reduces the flow around a swept wing to what is usually referred to as *infinite* swept wing flow or 2.5-dimensional flow. The formulation of the problem and description of the solver are presented in appendix A. Several investigations made use of LST either as design/validation tool for experimental investigations or as initial condition for parabolised stability equations (PSE) computations (e.g. Reibert *et al.* (1996); Arnal *et al.* (1998); Malik *et al.* (1999); Högberg & Henningson (1998); Haynes & Reed (2000)).

3.1. Formulation

The linear stability problem is presently solved using the Chebyshev spectral collocation method, with 100 polynomials. The spatial formulation is chosen where the flow disturbances are expressed in the waveform of equation 3.1,

$$\psi(x, y, z, t) = \phi(y) e^{i(\alpha x + \beta z - \omega t)} \quad (3.1)$$

where ω (angular frequency) is real, α (wavenumber along x) is complex and β (wavenumber along z) is real as no growth is assumed along the z direction based on the assumption of spanwise invariance.

Details on the derivation of the Orr-Sommerfeld (OS) equation for 2.5-dimensional flows are given by Mack (1984) (pp. 3-13). The companion matrix technique of Bridges & Morris (1984) is employed to overcome the eigenvalue nonlinearity. N factors (N) are computed as the integral of growth rates (i.e. the imaginary part of the chordwise wavenumbers: $-\alpha_i$) along x . Envelope N factors (N^{env}) are the x -integral of the local maximum values, per chord station, among all the considered modes (i.e. wavenumbers) (Arnal *et al.* 1998; Serpieri & Kotsonis 2016). Equation 3.2 gives the mathematical formulations of these two quantities,

$$N(x, \lambda_z, \omega) = \int_{x_0(\lambda_z, \omega)}^x -\alpha_i(\zeta, \lambda_z, \omega) d\zeta; \quad N^{env}(x, \omega) = \max_{\lambda_z} (N(x, \lambda_z, \omega)) \quad (3.2)$$

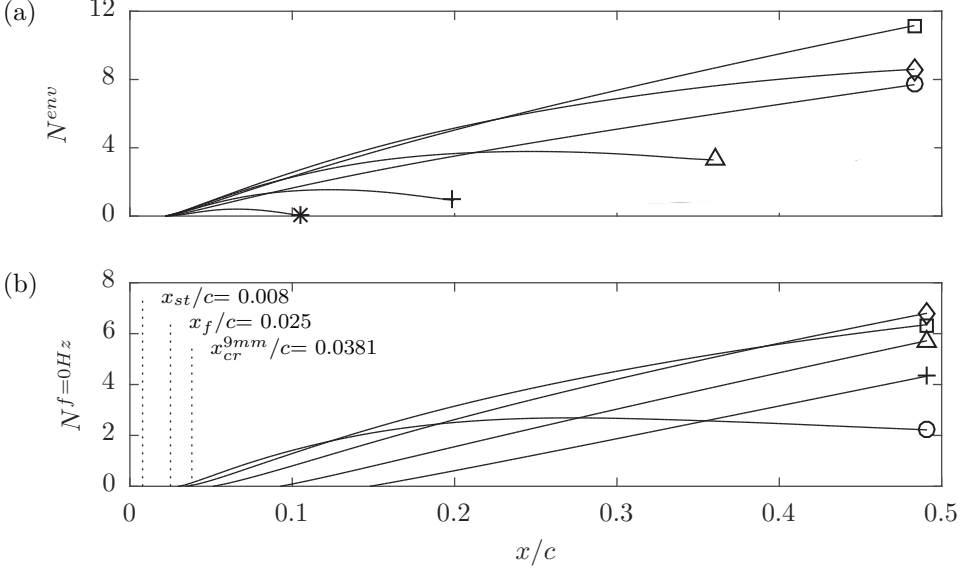


Figure 6: (a) Envelope N-factors for different frequencies (\circ : 0Hz; \square : 200Hz; \diamond : 400Hz; \triangle : 600Hz; $+$: 800Hz; $*$: 1000Hz). (b) N-factors of different stationary modes (\circ : $\lambda_z=5$ mm; \square : $\lambda_z=7$ mm; \diamond : $\lambda_z=9$ mm; \triangle : $\lambda_z=12$ mm; $+$: $\lambda_z=15$ mm). x_{st} indicates the stagnation point, x_f is the forcing location and x_{cr}^{9mm} is the critical station for the $\lambda_z = 9$ mm mode. See equations 3.2 for the formulation of the plotted quantities.

3.2. Results

The comparison of envelope N factors, between stationary and travelling modes of various frequencies is presented in figure 6a. Modes in the $0\text{Hz} \leq f \leq 600\text{Hz}$ frequency band show strongest amplification close to the stagnation point. While the $f=600\text{Hz}$ mode saturates at $x/c \approx 0.21$, the lower frequency waves are amplified throughout the boundary layer with the 200Hz mode being the most amplified mode. The fact that steady modes have lower growth than the travelling waves is a common outcome of LST analyses (Malik *et al.* 1999; Haynes & Reed 2000). Nevertheless, the eventual dominance of stationary modes over unsteady modes in practical cases is conditioned by the boundary layer receptivity to surface roughness and free stream turbulence, which is not accounted for in the LST eigenvalue problem. As such, while predicted by LST to be weaker, stationary vortices dominate the transition scenario in low turbulence flows (Deyhle & Bippes 1996).

Lastly, it is important to note that higher frequency modes are unstable only for shorter portions of the wing. For example, the $f=1000\text{Hz}$ mode is only weakly amplified near the leading edge and by station $x/c=0.113$ reaches $N^{env}=0$. Modes with higher frequency are either less amplified or they never destabilise in the current conditions. These preliminary results serve as an initial handle towards choosing the forcing frequency of the used plasma actuators. Specifically, the LST results suggest that unsteady forcing should be applied at frequencies that are higher than the shown unstable band.

A comparison between stationary modes with different wavelengths is shown in figure 6b. While in the most downstream regions the predicted instability is dominated by the $\lambda_z=9\text{mm}$ mode (see also Serpieri & Kotsonis (2016)), the smaller-wavelengths modes

Wavelength: λ_f (mm)	Forcing typology	Frequency: f_f (kHz)	Voltage: E (kV)
-	unforced	-	-
0	2D	2	3
9	3D critical	2	3
7	3D sub-cr.	2	3
12	3D super-cr.	2	3
9	3D cr. lower frequency	0.4	3
9	3D cr. lower amplitude	2	2

Table 1: Tested flow cases.

are dominating upstream as a consequence of the lower local Reynolds number. The DRE/UFD flow control strategy pivots on this phenomenon. Selective forcing of stationary modes with smaller wavelengths with respect to the eventually most amplified one, delays the amplification of the latter and consequently postpones the flow breakdown (Saric *et al.* 1998; Malik *et al.* 1999; Wassermann & Kloker 2002). For the presently studied flow, a stationary mode with spanwise wavelengths in the range of $\lambda_z=5\text{-}7\text{mm}$ should lead to this beneficial effects. The location of the stagnation point x_{st} , of the actuators x_f and the critical location for the $\lambda_z=9\text{mm}$ (x_{cr}^{9mm}) are also plotted.

It must be noted here that LST gives only indications of the pertinent modes evolution as it does not account for non-parallel and nonlinear effects. Furthermore, it does not account for the disturbances initial amplitude (i.e. the receptivity problem). Finally, neither the boundary layer nor the OS equation solver account for the model curvature and flow non-parallel effects. The effect of these parameters has been thoroughly analysed by Haynes & Reed (2000). Nonetheless, the outcomes discussed here give valuable information for the design of the employed flow control devices.

4. Test cases

Six forced flow cases are analysed in this study in addition to the unforced flow case. The first case corresponds to two-dimensional uniform forcing, enabled by a spanwise-invariant actuator. This is followed by three spanwise-modulated forcing cases at critical ($\lambda_f=9\text{mm}$), sub-critical ($\lambda_f=7\text{mm}$) and super-critical ($\lambda_f=12\text{mm}$) wavelengths. Notwithstanding the forced mode, the actuators were installed at identical locations ($x_f/c=0.025$). The actuators were supplied with a sinusoidal signal at $f_f=2\text{kHz}$ and with voltage amplitude of $E=3\text{kV}$ (i.e. voltage peak top peak of 6kV). The choice for the forcing frequency was based on the considerations in section 5.1. More specifically, the frequency was chosen to be 2kHz such to lie considerably above the LST-predicted unstable CFI band of $0 < f < 1000\text{Hz}$. In addition to the aforementioned cases a low frequency and low amplitude case were considered. For the low frequency case, the voltage amplitude is kept to $E=3\text{kV}$ but the frequency is reduced to 400Hz thus in the range of the amplified primary CFI (§ 3). For the low amplitude case, a signal of reduced voltage ($E=2\text{kV}$) and same frequency (2kHz) was inspected in order to elucidate the amplitude effects. The two additional cases were considered only for the critical wavelength actuator ($\lambda_f=9\text{mm}$). The parameters of the tested cases are summarised in table 1.

5. Actuator characterisation

In this section, the mechanical performance of the used actuators is quantified. The spanwise-uniform 2-D actuator is chosen for this analysis, simplifying the flow field to a two-dimensional arrangement. The identified amplitude effects are expected to reasonably describe the performance of the spanwise-modulated actuators, considering that their electrode width (w) remains constant. The characterisation is carried out in quiescent flow. Planar high-speed PIV was employed to measure the induced velocity and compute the actuator body-force and the related thrust (for details on the body-force extraction methods see Kotsonis *et al.* (2011) and Kotsonis (2015)). Furthermore, spectral analysis of the unsteady flow field is presented to infer the unsteady flow field induced by the actuators.

5.1. Experimental set-up

The camera, laser and synchronisation equipment used for this experiment are the same as described in 2.4. For this experiment, the camera's active sensor was reduced to $960 \times 440\text{px}^2$ to increase its maximum frame rate. The camera was equipped with a Nikon Nikkor 200mm macro lens operated at $f_{\#}=8$. The magnification factor was $M=1.14$. The air in the closed box was seeded with droplets of paraffin oil, $1\mu\text{m}$ in average diameter, generated by a *TSI Atomizer* nozzle. The coordinate system used in this experiment is represented by the symbols $x_p y_p z_p$ (see figure 3b). The system is arranged such that the x_p axis is in the direction of the induced jet (i.e. orthogonal to the electrodes length), the y_p is perpendicular to the plane of the actuator and z_p is along the length of the electrodes. The plasma actuator was installed in a transparent acrylic glass box enclosing a volume of 0.25m^3 (1m long along x_p). The plane inspected with PIV is aligned with $x_p - y_p$, given the uniformity of the induced flow field along z_p . The laser, camera and transparent box were installed on a pneumatically stabilised table (i.e. an optical table) to avoid vibrations on the set-up which could be detrimental for such high magnification planar PIV experiment. Cross-correlation was carried out with final interrogation windows of $24 \times 24\text{px}^2$ with relative overlap set to 75%. As such, the final vector spacing was approximately 0.053mm in both x_p and y_p directions. The system was operated at acquisition rate of 10kHz in single-frame mode thus the pulse separation between the correlated frames was $100\mu\text{s}$. Sequences of 25000 images were acquired for each test case for a total measurement time of 2.5s. The measurement started prior to plasma actuation thus capturing the initial flow acceleration phase.

5.2. Performance

In quiescent flow environments, when the actuator is supplied with the voltage signal, the strong electric field established between the electrodes ionises and accelerates the air molecules. The incompressible Navier-Stokes momentum equation is used to retrieve the induced body-force. In this very initial regime, advection, diffusion and pressure terms are negligible with respect to the unsteady acceleration and body-force terms. Following Kotsonis *et al.* (2011), under the specified assumptions, the momentum equation reduces to $\mathbf{F} = \rho \partial \mathbf{U} / \partial t$, where \mathbf{F} is the body-force and \mathbf{U} the velocity. Low-pass filtering of the measured velocity signal was applied in order to eliminate high frequency oscillations associated with the AC voltage frequency. In addition to the body-forces, the time-averaged velocity field is computed, after the induced jet has fully developed, from the measured time series and presented in figure 7 $f_f=2\text{kHz}$ - $E=3\text{kV}$.

The induced jet originates in the vicinity of the inner edge of the exposed electrode and is mainly aligned with the x_p direction. The wall-normal velocity component, at the

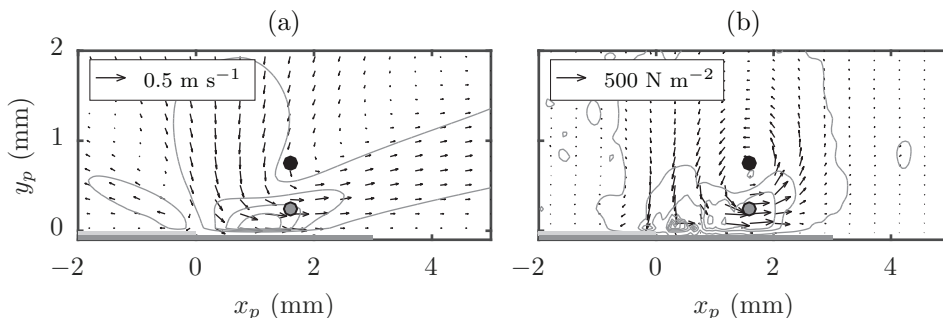


Figure 7: (a) Time-averaged velocity magnitude field (grey solid lines: 5 levels, from 0 to 0.6 m s^{-1}). (b) Body-force magnitude field (grey solid lines: 5 levels, from 50 to 1000 N m^{-2}). Vectors: $x_p - y_p$ components of the respective contour variables (reference vector in the upper left corner). AC-DBD actuator operated at $f_f=2\text{kHz}$ - $E=3\text{kV}$. The two horizontal grey lines below $y_p=0$ represent (to scale) the electrodes of the actuator. The markers at $x_p=1.6\text{mm}$ - $y_p=0.25$ (grey) and 0.75mm (black) refer to figure 8.

electrodes interface, supplies the mass for the wall-parallel jet (Kotsonis *et al.* 2011). A secondary wall-parallel jet, oriented opposite to the main velocity, is observed on top of the exposed electrode. This secondary jet is not observed with the usual copper electrode actuators and can be caused by the extremely low thickness of the employed actuators building up a competing electrical field. A confined region of negative x_p -body-force is also observed. The body-force field is overall rather weak, for the tested conditions, and predominant along the x_p direction (Kotsonis 2015).

Spatial integration of the body-force field retrieves the exerted specific (i.e. per actuator unit length) thrust. This is eventually used to compute the momentum coefficient, according to equation 5.1, which is used to compare the actuators authority for the different forcing conditions,

$$C_\mu = \frac{T_{x_p}}{\frac{1}{2} \rho u_e^2 \vartheta_u} \quad (5.1)$$

where the local (at the actuator position) boundary layer edge velocity $u_e=14 \text{ m s}^{-1}$ and momentum thickness $\vartheta_u=7.81 \cdot 10^{-2} \text{ mm}$ are extracted from the boundary layer numerical solution for the investigated case (see appendix A).

The thrust generated by the plasma actuator along x_p and the respective momentum coefficient for the different test cases considered in this study are presented in table 2. When the actuator is operated at $f_f=2\text{kHz}$ - $E=3\text{kV}$, the horizontal component of the thrust generated is $T_{x_p}=0.432 \text{ mN/m}_{act}$ and the momentum coefficient is $C_\mu=0.046$. This is the combination of supplied voltage and frequency that leads to the strongest induced jet. When the frequency is reduced to 400Hz , the performance of the actuator is reduced. Similarly, decreasing the voltage amplitude to 2kV at the same operated frequency of 2kHz , lowers C_μ .

For all the investigated configurations of table 2, the generated thrust is comparatively less than what reported by Chernyshev *et al.* (2013) and Dörr & Kloker (2015b) in their studies. However, in the current study, the AC-DBD plasma jets are used in a respective fashion to isolated roughness elements for DRE/UFD flow control. In such a configuration, the actuators are used to induce a weak localised perturbation of the incoming flow thus requiring only moderate forcing amplitudes. The specific

Voltage E (kV)	Frequency f_f (kHz)	T_{x_p} (mN/m _{act})	C_μ
3	0.4	0.0118	0.013
2	2	0.351	0.037
3	2	0.432	0.046

Table 2: AC-DBD actuator induced thrust and momentum coefficient.

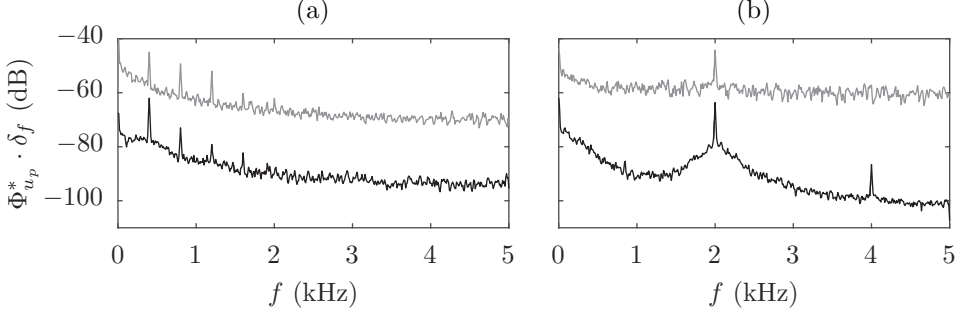


Figure 8: Non-dimensional normalised power spectra of the actuators induced velocity u_p ($\Phi_{u_p}^* \cdot \delta_f / U_\infty^2$, see equation 2.1, $\delta_f = 10$ Hz) at the position of the markers ($x_p = 1.6$ mm - $y_p = 0.25$ (grey) and 0.75 mm (black)) in figure 7 (grey curve displaced by +10 dB for visualization). (a) $f_f = 0.4$ kHz - $E = 3$ kV, (b) $f_f = 2$ kHz - $E = 3$ kV.

thrust applied by the actuators used by Dörr & Kloker (2017) for the same purpose, is comparable to the values reported here.

Capitalising on the high sampling rate of the employed PIV method, access to the unsteady and spectral features of the plasma-induced flow field is gained. Spectral analysis of the velocity fluctuations, at two points at $x_p = 1.6$ mm - $y_p = 0.25$, 0.75 mm (markers in figure 7(a)), was carried out for the two different frequencies at which the actuators were operated (0.4 and 2 kHz). The results are shown in figure 8. The spectra are normalised according to equation 2.1 and non-dimensionalised with U_∞^2 thus they directly show the relative kinetic energy per frequency band. They reveal strong unsteady fluctuations at the respective carrier frequency as well as higher harmonics. Moreover, low frequency fluctuations close to the wall are observed. These can be attributed to a range of factors including plasma-induced thermal disturbances, measurement noise and unstable plasma formations. The exact origin of these fluctuations should be taken into account in the future for a complete characterisation of the plasma effect. Moreover, it is currently unclear to what extent these low frequency fluctuations would be present also on the wing mounted configuration under external flow condition. Such study will require a dedicated effort that goes beyond the scope of this article.

6. Infrared flow visualisation

In this section, flow visualisation results using IR thermography are presented. The IR fields will be used to inspect the effectiveness of the developed actuators in conditioning the stationary CFI modes. For all discussed results, geometrical mapping of the captured images was applied to account for the curvature of the model and the perspective effects from the camera.

The IR flow visualisation for the natural transition flow (i.e. with no boundary

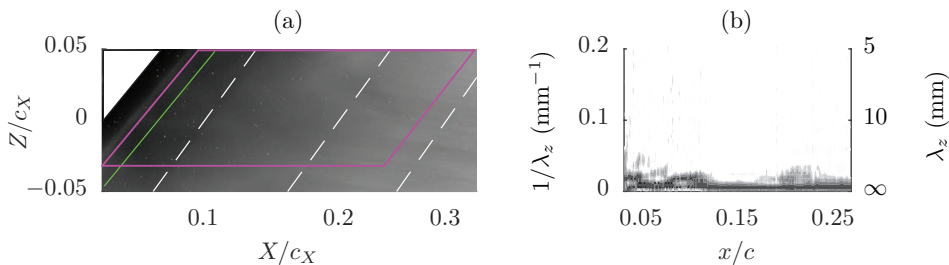


Figure 9: Natural transition flow case. (a) IR thermography fields. The flow comes from left. The solid (green) line divides the figure in two regions where different contrast levels are used. The dashed white lines are constant chord lines at $x/c=0.1, 0.2$ and 0.3 . The region enclosed with the solid (magenta) lines refers to figure 9b. (b) Wavenumber power spectral density of the IR pixels intensity along the chord. The analysis is performed in the region within the solid (magenta) lines of figure 9a.

layer forcing) is presented in figure 9a. To enhance the signal-to-noise ratio of the measurements, time averaging of the captured thermography fields was performed over the sampled period (300 samples). The flow shows strong homogeneity in both the spanwise and chordwise directions. For the considered model (i.e. geometry and surface roughness), angle of attack, Reynolds number and free stream turbulence level, no strong CFI modes are amplified in the inspected range and the boundary layer remains laminar until the most downstream station inspected. To further analyse the spatial and spectral arrangement of the boundary layer from the IR image, the individual pixel intensities within the solid (magenta) lines depicted in figure 9a were sampled and analysed in the wavenumber spectral domain. This procedure was performed along constant chord lines. The power spectral density (Φ) was computed using Welch's algorithm (Welch 1967). The wavenumber resolution of the spectra is 0.006mm^{-1} . The results are presented in figure 9b. No stationary modes appear above the measurement noise level for the unforced flow case.

The IR fields for the four actuators operated at $f_f=2\text{kHz}$ - $E=3\text{kV}$ ($C_\mu=0.046$) are shown in figure 10. The plasma regions initiated by the actuators are clearly visible in the images close to the leading edge as localised regions of increased thermal radiation. This is mainly attributed to a weak heating effect of the model surface directly beneath the plasma formation as reported by Kotsonis (2015). In the case of spanwise-uniform forcing (figure 10a), the plasma manifests as a bright continuous line in the z direction. When the spanwise-modulated forcing is applied (figures 10b,c and d), the localised plasma regions spaced at the respective forced wavelength appear as a sequence of bright spots. Due to the high IR intensity of the plasma formation, intensity equalisation (de-saturation) has been applied to facilitate observation of IR intensity distribution downstream of the actuators (the solid (green) line in the fields divide the images in two regions with different contrast settings).

For the two-dimensional forcing, the flow does not exhibit significant alteration of the stationary vortices, compared to the unforced case. Eventually, moving more downstream, stationary waves do take place however their intensity and spacing appear uneven along lines parallel to the leading edge. No clear transition fronts, within the imaged FOV are evident in this flow case. When spanwise-modulated forcing is applied, the thermal footprint of primary instability modes becomes more visible in the IR fields. The resulting streaks appear locked to the spacing and the position of the plasma regions. Their relative

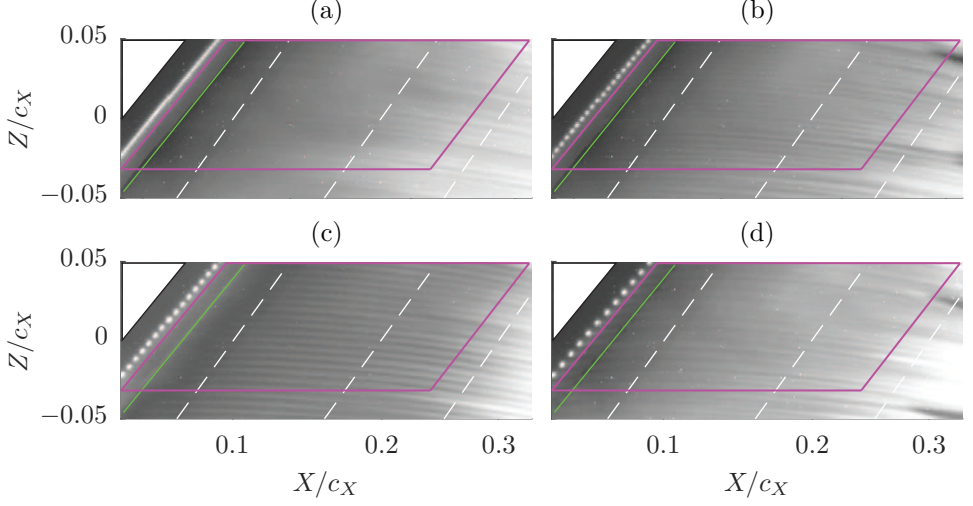


Figure 10: IR thermography fields. Actuators operated at $f_f=2\text{kHz}$ - $E=3\text{kV}$ ($C_\mu=0.046$): (a) Spanwise-uniform forcing; (b) sub-critical forcing ($\lambda_f=7\text{mm}$); (c) critical forcing ($\lambda_f=9\text{mm}$); (d) super-critical forcing ($\lambda_f=12\text{mm}$). The regions enclosed with the solid (magenta) lines refer to figure 11.

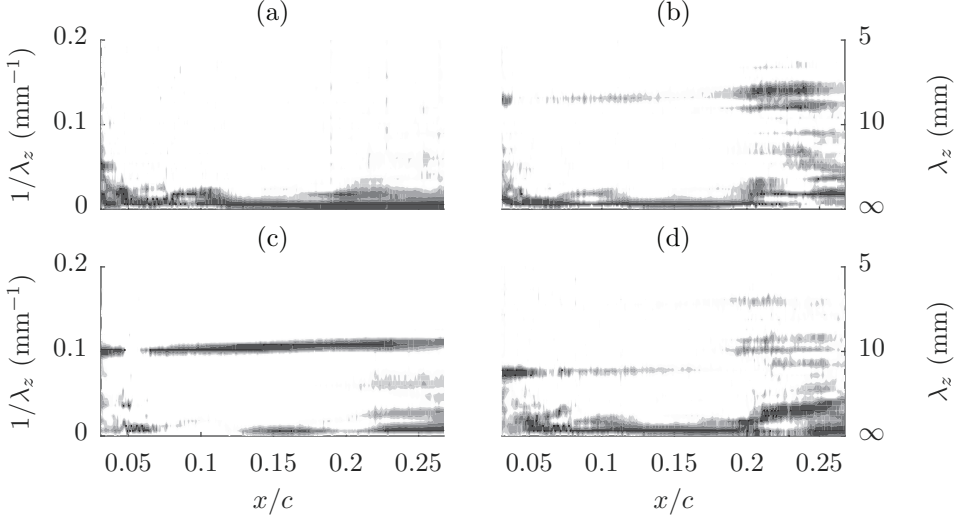


Figure 11: Wavenumber power spectral density of the IR pixels intensity along the chord. Same cases as figure 10.

intensity is also more uniform along constant-chord lines, further suggesting conditioning of both wavelength and amplitude of the stationary cross-flow vortices by the plasma actuator. Overall, for the spanwise-modulated forcing, a more uniform flow topology is established with evident monochromatic structures present in the more upstream portion of the wing. Additionally, in figures 10b and d the appearance of turbulent wedges at the most downstream portions of the FOV suggests advancement of the transition front due to actuation.

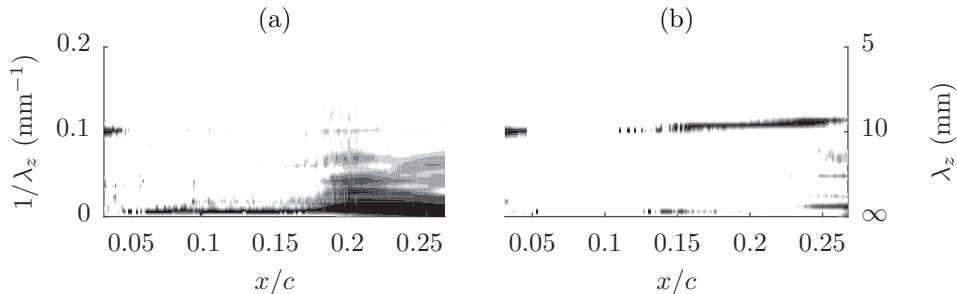


Figure 12: Wavenumber power spectral density of the IR pixels intensity along the chord. $\lambda_f=9$ mm actuator operated at: (a) $f_f=0.4$ kHz - $E=3$ kV ($C_\mu=0.013$); (b) $f_f=2$ kHz - $E=2$ kV ($C_\mu=0.037$).

The IR pixels intensity spectra for the flow cases of figure 10 are presented in figure 11. When spanwise-uniform forcing is applied, no dominating stationary modes are present in the upstream portion of the FOV similar to the unforced flow case of figure 9. In the most downstream region, the spectrum shows weak energy levels corresponding to the development of some coherent streaks as shown in figure 10a. When spanwise-modulated forcing is applied, the wavenumber spectra reveal the presence of harmonic peaks closely aligned to the forced wavelength. Comparing the spectra of figures 11b-d to the respective IR images in figures 10b-d it becomes apparent that the selective forcing at the plasma wavelength effectively conditions the formation of the stationary cross-flow vortices at approximately the same wavelength. This is especially evident for the $\lambda_f=7$ mm and 9mm actuators fields. Moreover, it is shown that the critical mode ($\lambda_z=9$ mm) is the most receptive to leading edge forcing, showing the highest spectral energy levels throughout the inspected domain. When the sub-critical $\lambda_z=7$ mm waves are forced (figures 11b), the most downstream portion of the domain shows a much broader spectrum with longer wavelengths modes being amplified. Finally, when the $\lambda_z=12$ mm mode is forced (figures 11d), stationary waves at the forced wavelength are amplified. From $x=0.19c$, a super-harmonic mode with double wavenumber (wavelength of ≈ 6.1 mm) is also captured. Amplification of superharmonic modes is a commonly observed feature in CFI boundary layers (Reibert *et al.* 1996) related to nonlinear interaction between primary modes (Haynes & Reed 2000). Energy at wavelengths of 10mm and 9mm is also captured downstream of $x=0.19c$.

The wavenumber spectra equivalent to those presented in figure 11 are presented in figure 12 for the spanwise-modulated actuator of $\lambda_f=9$ mm operated at the lower (400Hz) frequency and at the lower voltage (2kV). When the actuator is operated at $E=3$ kV - $f_f=400$ Hz ($C_\mu=0.013$) (figure 12a), spectral energy at the forced wavelength (9mm) is weakly observed only in the range $0.18 \leq x/c \leq 0.22$ however this mode does not dominate the boundary layer and longer-wavelength modes are strongly amplified. The apparent weakness of the spectral coherence in this case, is attributed to the frequency of the applied forcing, which falls in the band of the primary travelling modes as predicted by LST (figure 6a). In these conditions, the eventual presence of strongly amplified unsteady vortices dominate over the stationary CFI. Furthermore, at these operational parameters, the momentum coefficient of the actuator (table 2) attains the lowest values among the tested cases. For the $E=2$ kV - $f_f=2$ Hz ($C_\mu=0.037$) case (figure 12b), the spectrum replicates similar features of the $E=3$ kV - $f_f=2$ Hz ($C_\mu=0.046$) case (see figure 11(c)) albeit with lower energy levels. This indicates the possibility of adjusting the forcing

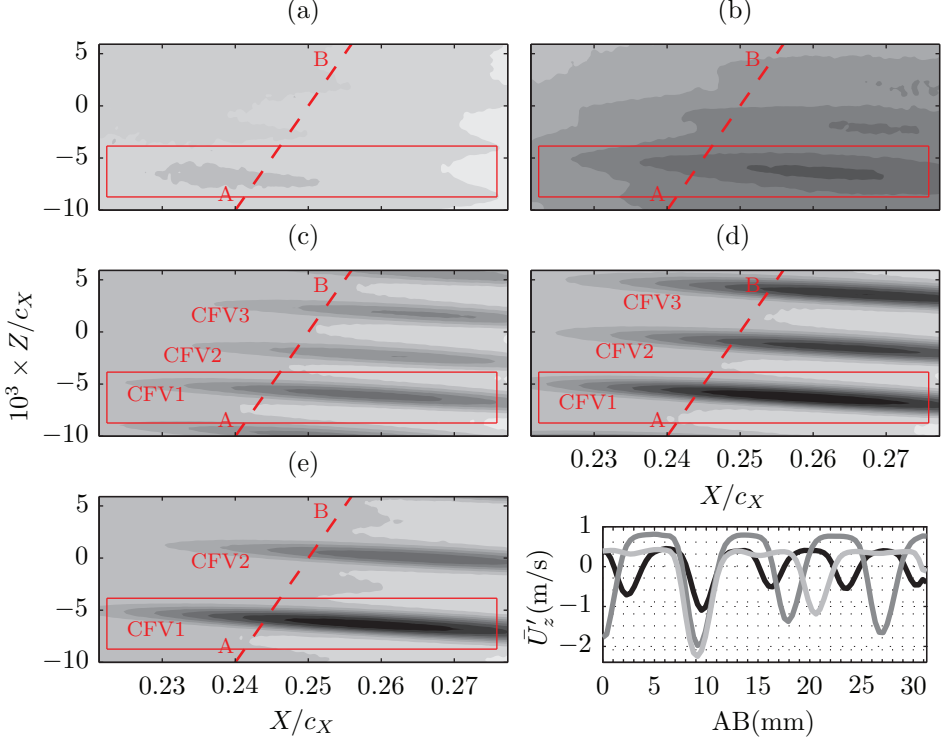


Figure 13: Time-averaged U velocity fields (10 levels, from 0.84 (black) to $1U_\infty$ (white)). The flow comes from left. (a) actuator non operated; (b) spanwise-uniform forcing; (c) sub-critical forcing ($\lambda_f=7\text{mm}$); (d) critical forcing ($\lambda_f=9\text{mm}$); (e) super-critical forcing ($\lambda_f=12\text{mm}$). Actuator operated at $f_f=2\text{kHz}$ - $E=3\text{kV}$ ($C_\mu=0.046$). The (red) lines and labels refer to analyses presented in the remainder. Inset: spanwise-fluctuation of the \bar{U}_z' velocity signal sampled along the line AB in fields: (c) black, (d) dark grey, (e) light grey line.

amplitude of the actuators by tuning the supplied voltage, corroborating the observations of Schuele *et al.* (2013) (further analysed in the remainder).

7. Velocity field

In this section, the results of the high-speed PIV investigations are presented. The effect of the plasma forcing on the primary instability is quantified by means of the velocity field statistics. The spatio-temporal evolution of the unsteady flow field is further elucidated through spectral and proper orthogonal decomposition (POD) analyses.

7.1. Time-averaged flow topology

The time-averaged U velocity fields for the different test cases are presented in figure 13. Figure 13a shows the unforced flow. The actuator is mounted on the wing but is not supplied with voltage. The boundary layer, within the imaged domain, is still laminar and slightly modified by natural CFI mechanisms as seen in figure 9a. The appearance of stationary vortices is observed in the presented velocity field as a weak velocity modulation along the span.

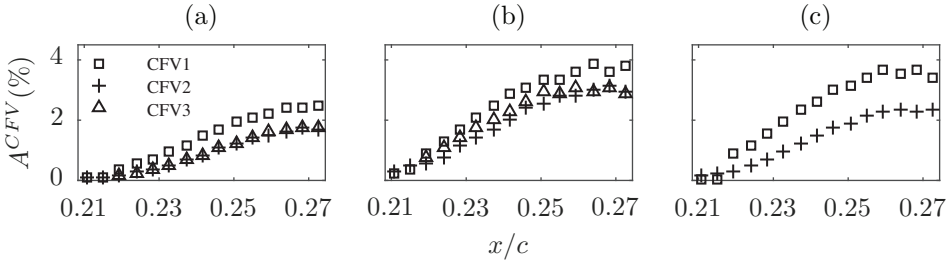


Figure 14: Spatial evolution of the individual vortices of figure 13c, d and e computed from equation 7.1. (a) sub-critical forcing ($\lambda_f=7\text{mm}$); (b) critical forcing ($\lambda_f=9\text{mm}$); (c) super-critical forcing ($\lambda_f=12\text{mm}$).

When two-dimensional forcing is applied (figure 13b), the flow drastically rearranges. The overall magnitude of velocity is reduced, showing a thickening of the boundary layer. Moreover, the velocity local minima are now more distinguishable, suggesting the enhancement of the stationary primary vortices. When spanwise-modulated forcing is applied (figure 13c,d and e), separate and more uniform stationary vortices become clearly visible. The spanwise spacing, along a line parallel to the leading edge (segment AB in the contours) can be compared to the actuated wavelength. The velocity spanwise fluctuations (\bar{U}'_z) are presented in the inset of figure 13, further reconciling with the outcomes of the flow visualisation experiment of § 6. When the super-critical mode ($\lambda_f=12\text{mm}$) is forced, the superharmonic mode seen before in figure 11c becomes evident, downstream of $x/c=0.25$, in the regions in between the stronger CFVs. The lower side of the presented flow fields always shows lower velocities in comparison to the upper region. This effect is attributed to a possible small inclination of the laser sheet (i.e. rotation about the X axis), such that the lower illuminated region is slightly closer to the wall.

Inspecting the fields pertaining to the three different forced wavelengths shows that, when critical forcing is applied, the vortices appear more developed than the sub-critical and super-critical forcing cases. In fact it can be seen that the velocity minima corresponding to the low-momentum region attain the lowest values for the $\lambda_z=9\text{mm}$ vortices. In addition, the spatial evolution of the stationary waves can be quantified by computing their amplitude as defined by equation 7.1 (White & Saric (2005) and Serpieri & Kotsonis (2016)),

$$A^{CFV}(x) = z_{rms} \{ \bar{U}'_z(x)/U_\infty \} |_{y_t=y_t^{PIV}} \quad (7.1)$$

As evident in figure 13, ensembles of two to three individual vortices are available through the PIV measurements. Due to the fixed FOV, the number of fully resolved vortices is dependent on the forcing wavelength. For the calculation of the amplitudes, the individual vortices are tracked in their spatial evolution. The estimated amplitudes for the individual vortices in the spanwise-modulated forcing cases (figure 13c-e) are shown in figure 14a-c respectively.

Within the imaged field, the stationary vortices show similar growths despite the different amplitudes. Forcing the critical mode at $\lambda_f=9\text{mm}$ leads to more developed waves compared to the other two modes, especially with respect to the sub-critical mode, in both initial amplitude and spatial amplification. These results, which match with the stronger energy shown for this mode in the IR spectra (figure 11), confirm that forcing sub-critical modes lead to less amplified stationary vortices (see e.g. Reibert *et al.* (1996), Malik *et al.* (1999) and Wassermann & Kloker (2002)). All the fields show monotonic

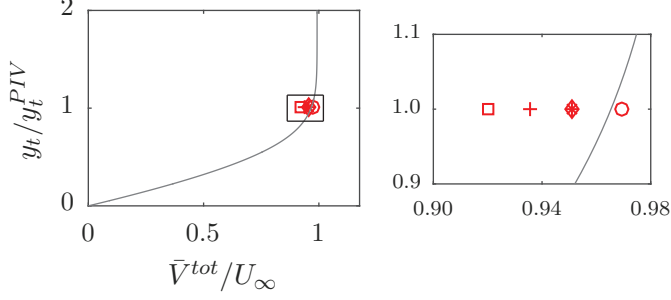


Figure 15: Comparison between the measured spanwise-mean velocity magnitude ($z_{mean}\{\bar{V}^{tot}\}|_{y_t=y_t^{PIV}}$) from the velocity fields of figure 13 (symbols) and the boundary layer numerical solution (solid line) at $x/c=0.25$. (○) actuator non operated; (□) spanwise-uniform forcing; (*) sub-critical forcing ($\lambda_f=7\text{mm}$); (+) critical forcing ($\lambda_f=9\text{mm}$); (◇) super-critical forcing ($\lambda_f=12\text{mm}$). Inset: magnified view.

growth of the stationary vortices. However, the amplitudes appear to saturate at the most downstream portion of the fields. This is expected from boundary layers dominated by stationary CFVs undergoing laminar-to-turbulent transition (Haynes & Reed 2000; Serpieri & Kotsonis 2016). However, it has to be clarified here that performing this analysis on planes at constant distance from the model wall has some limitations. In fact, moving downstream, the stationary waves grow and so does the boundary layer (see the schematic of figure 5). Hence, moving downstream at a constant wall-normal position, the measurement plane intersects the stationary vortices in a lower region where the velocity modulation effect is milder. This results, when using the metrics of equation 7.1, in lower amplitudes. Therefore the growth rates of the stationary CF vortices should be retrieved from full three-dimensional fields (Reibert *et al.* 1996; Haynes & Reed 2000; White & Saric 2005; Wassermann & Kloker 2002; Serpieri & Kotsonis 2016). Despite these observations, the effect is rather mild within small chordwise domains, such as the one considered here.

An additional consideration in the analysis of figure 14, relates to the fact that the mean-flow distortion of the considered fields caused by the primary CFVs is not even. In fact, more developed vortices modify the mean flow more significantly. A way to inspect this effect is proposed here by comparing the measured spanwise-mean velocity magnitude ($z_{mean}\{\bar{V}^{tot}\}|_{y_t=y_t^{PIV}}$) from the velocity fields of figure 13 (sampled along the AB segment) and the undisturbed boundary layer numerical solution (described in appendix A). The outcomes of this comparison are presented in figure 15. Evidently, the boundary layer corresponding to the spanwise-uniform and spanwise-modulated critically forced ($\lambda_f=9\text{mm}$) flows underwent significant mean flow distortion. The unforced flow case as well as the super-critical ($\lambda_f=12\text{mm}$) and sub-critical ($\lambda_f=7\text{mm}$) forcing cases are distorted more mildly. The measured unforced boundary layer agrees relatively well with the numerical prediction. The slight discrepancy is attributed to modelling assumptions in the boundary layer solution as well as measurement uncertainties in the PIV fields.

The time-averaged velocity field for the additional forcing case of the critical mode actuator operated at the lower frequency (400Hz) and same voltage amplitude (3kV, $C_\mu=0.013$) is presented in figure 16a. The velocity field shows a spanwise modulation with amplified stationary vortices at different wavelengths. When the actuator is operated at $f_f=2\text{kHz}$ - $E=2\text{kV}$ ($C_\mu=0.037$) (figure 16b), the boundary layer features weaker stationary vortices when compared to the $f_f=2\text{kHz}$ - $E=3\text{kV}$ case (figure 13(d)). This

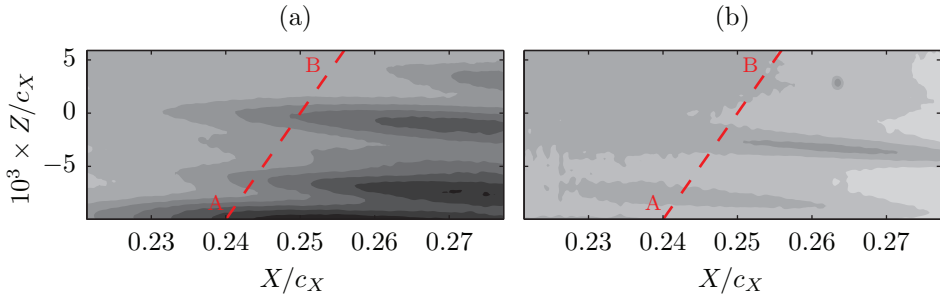


Figure 16: Time-averaged U velocity fields (10 levels, from 0.84 (black) to $1U_\infty$ (white)). (a) $f_f=0.4\text{kHz}$ - $E=3\text{kV}$ ($C_\mu=0.013$); (b) $f_f=2\text{kHz}$ - $E=2\text{kV}$ ($C_\mu=0.037$).

further confirms the dependency of forced cross-flow vortex strength to the momentum coefficient of the actuator.

A comparison of the present study to the passive control investigation of Serpieri & Kotsonis (2016), is shown in figure 17. In this previous work, the critical cross-flow instability mode was conditioned with leading edge micron-sized roughness elements (diameter: $d_r=2.8\text{mm}$, height: $k_r=10\mu\text{m}$) installed at the same chordwise position as the plasma actuators in the present study ($x/c=0.025$). The velocity profile was acquired with hot-wire scans. Note that the velocity measured in that experiment, coincides mainly with $\sqrt{U^2 + V^2}$, however, given the strong predominance of the U component (Serpieri & Kotsonis 2016), this comparison can still be valid. The comparison demonstrates that, when the actuator is operated at $f_f=2\text{kHz}$ - $E=3\text{kV}$ ($C_\mu=0.046$), the spanwise-averaged value of the mean velocity attains the lowest value among all cases. For the lower frequency case, the lower velocity value compared to the laminar solution is explained by the more advanced transitional status of the forced boundary layer. When the actuator was operated at 400Hz, the boundary layer showed multiple stationary modes (figure 12a) and enhanced fluctuations (see the discussion of figure 20a). Moving to the other flow cases, the comparison with the passive roughness elements used by Serpieri & Kotsonis (2016) is more instructive given the CFI monochromatic state of the compared boundary layers. The hot-wire profile shows already at this chordwise station a small deviation from the laminar profile, caused by the mean-flow distortion (Serpieri & Kotsonis 2016). Moreover, the profile crosses the station of the current PIV measurements ($y_t=1.5\text{mm}$) between the velocity values of the tested voltages thus showing that the $d_r=2.8\text{mm}$ - $k_r=10\mu\text{m}$ passive roughness has a milder effect on the boundary layer than the $f_f=2\text{kHz}$ - $E=3\text{kV}$ ($C_\mu=0.046$) active roughness but stronger compared to the $f_f=2\text{kHz}$ - $E=2\text{kV}$ ($C_\mu=0.037$) case.

7.2. Flow fluctuations

As demonstrated in section 5.2, the employed plasma actuators produce an inherently fluctuating forcing effect, at a frequency aligned to the oscillation of the AC high-voltage signal. The effect of this unsteady forcing on the boundary layer is investigated in this section. Dörr & Kloker, in their studies (Dörr & Kloker (2015b, 2016)) (Reynolds number based on plate length and free stream velocity orthogonal to the leading edge $Re=92000$), showed very little direct effect of unsteady forcing on the unsteady instability modes. The actuators in the aforementioned studies were modelled with stationary or periodic high frequency body-force inputs in their numerical setup. However, in the case of unsteady force, the actuators were operated at a frequency more than four times higher than

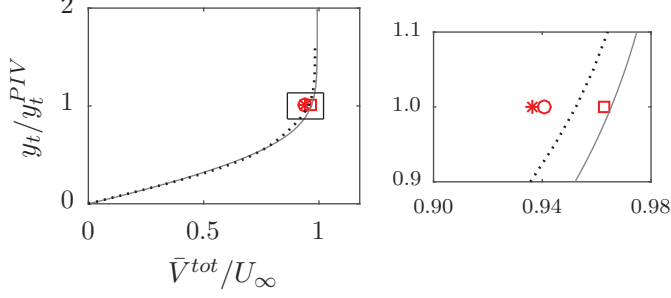


Figure 17: Comparison between the measured spanwise-mean velocity magnitude ($z_{mean}\{\bar{V}^{tot}\}|_{y_t=y_t^{PIV}}$) from the velocity fields of figure 16 (symbols), the boundary layer numerical solution (solid line) at $x/c=0.25$. Critical forcing ($\lambda_f=9\text{mm}$): (\circ) $f_f=0.4\text{kHz}$ - $E=3\text{kV}$ ($C_\mu=0.013$); (\square) $f_f=2\text{kHz}$ - $E=2\text{kV}$ ($C_\mu=0.037$); ($*$) $f_f=2\text{kHz}$ - $E=3\text{kV}$ ($C_\mu=0.046$). Dotted line: $d_r=2.8\text{mm}$ - $k_r=10\mu\text{m}$ passive roughness (Serpieri & Kotsonis 2016). Inset: magnified view.

the frequency of the pertinent *type-I* secondary instability mode. The present study is conducted at a higher Reynolds number (chord Reynolds number $Re = 1.08 \cdot 10^6$), at which the respective mode peaks at a frequency of 5.5kHz (Serpieri & Kotsonis 2016). In the current experimental framework, achieving frequencies four times larger than the *type-I* mode frequency was technically unfeasible. This restriction was already envisioned by Dörr & Kloker as a possible limitation for UFD-LFC with AC-DBD actuators for high Reynolds numbers flows. Based on the above considerations, it was chosen to operate the actuators of the present study at a frequency of 2000Hz . Such frequency is beyond the primary travelling modes band ($0 < f < 1000\text{Hz}$), yet below the frequency range corresponding to secondary instabilities ($f > 4000\text{Hz}$) (Serpieri & Kotsonis 2016).

7.2.1. Statistical analysis

The statistic fluctuations fields, for the test cases presented in figure 13, are presented in figure 18. The overall level of velocity fluctuations for the unforced flow (figure 18a) is very low. In contrast, spanwise-uniform forcing dramatically enhances the unsteady field (figure 18b). This flow case was chosen to investigate the effects that the employed unsteady forcing has on the boundary layer. The higher level of fluctuations in conjunction to the thickening of the boundary layer discussed before suggest that this flow is in a more advanced transitional state compared to the unforced case.

When spanwise-modulated forcing is applied (18c,d and e for sub-critical, critical and super-critical wavelengths, respectively), the flow fluctuations appear enhanced only in the regions of the conditioned stationary vortices. This is expected in boundary layers dominated by stationary cross-flow vortices as the latter introduce strong velocity shears (Kawakami *et al.* 1999; Malik *et al.* 1999; White & Saric 2005; Bonfigli & Kloker 2007). The lower level of fluctuations for the sub-critical mode suggests a more stable flow in line with the DRE/UFD control strategies (this aspect will be addressed later in § 7.2.4).

7.2.2. Spectral characteristics

Time series of the U'_t velocity signal sampled along the AB segment at $x/c=0.25$ of figures 13 and 18 are analysed in the Fourier domain. The power spectra are computed using Welch's method (Welch 1967) with a final frequency resolution of $\delta_f=10\text{Hz}$. The spectra are normalised according to equation 2.1 and non-dimensionalised with U_∞^2 . The results are presented in figure 19 for the five flow cases of figures 13 and 18. While the

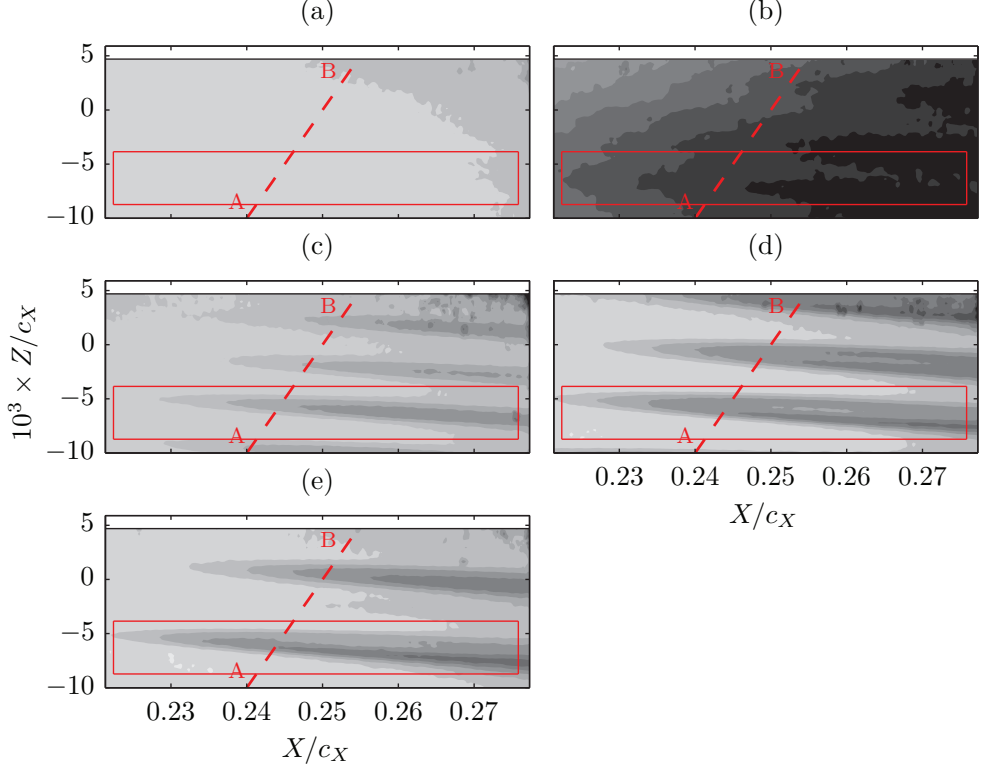


Figure 18: Standard deviation of U velocity fields (10 levels, from 0 (white) to $0.0784U_\infty$ (black)). (a) actuator non operated; (b) spanwise-uniform forcing; (c) sub-critical forcing ($\lambda_f=7\text{mm}$); (d) critical forcing ($\lambda_f=9\text{mm}$); (e) super-critical forcing ($\lambda_f=12\text{mm}$). Upper region masked for higher measurement noise.

unforced flow shows very low spectral energy in all the resolved band ($0\text{Hz} \leq f \leq 1500\text{Hz}$), the spanwise-uniform actuation results in very pronounced fluctuations in the band $0\text{Hz} \leq f \leq 350\text{Hz}$. This is somewhat unexpected as the operated AC voltage is fixed at the frequency of $f_f=2000\text{Hz}$ which is well beyond the corresponding band of travelling modes at these flow conditions (cfr. § 3). While at this point the analysis is inconclusive, it is likely that either low frequency fluctuations directly introduced by the actuator (recall the results of section 5.2) or nonlinear interactions between the plasma-induced jets and the boundary layer modes take place in the unsteady velocity field, thus enhancing the fluctuations energy in the travelling CF waves band. Moreover, the spanwise uniformity of the unsteady forcing is also present in the spectra. This is a direct consequence of the absence of amplified steady vortices in this flow field as seen in the statistics fields (figure13b).

Analysis of the spanwise-modulated actuated flows shows that the fluctuations are modulated along the span directly corresponding to the position of the conditioned cross flow vortices. They attain considerable energy throughout the resolved spectrum, albeit stronger at the lower frequencies. Among the different spanwise-modulated actuators, the 9mm and 12mm wavelength actuators are responsible for the strongest fluctuations. The Nyquist frequency of the implemented PIV measurements is lower than the secondary instability band (Serpieri & Kotsonis 2016) and hence the secondary instability mecha-

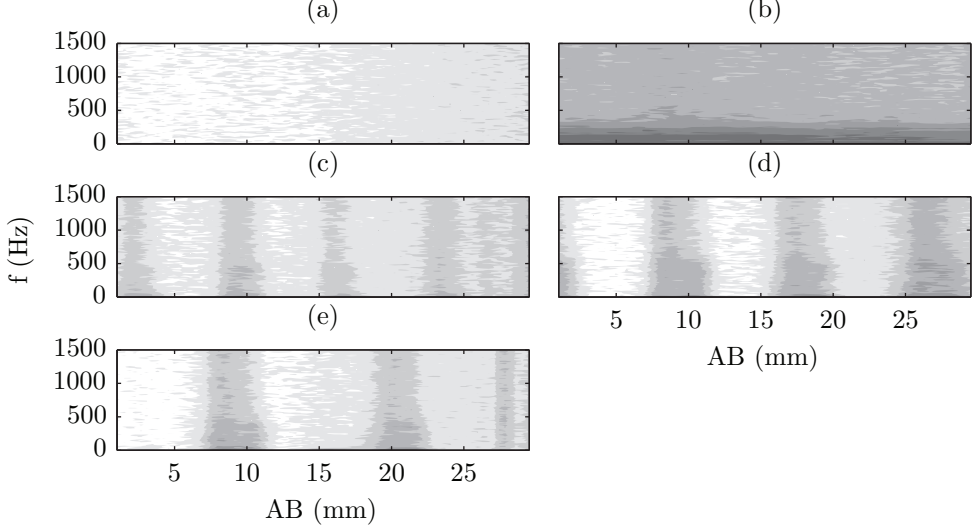


Figure 19: Non-dimensional normalised power spectra ($\Phi_{U'_t}^* \cdot \delta_f / U_\infty^2$, see equation 2.1, $\delta_f=10\text{Hz}$) of the U'_t velocity signal sampled along the AB line at $x/c=0.25$ of figures 13 and 18 (10 levels, from -60 (white) to -30dB (black)). (a) actuator non operated; (b) spanwise-uniform forcing; (c) sub-critical forcing ($\lambda_f=7\text{mm}$); (d) critical forcing ($\lambda_f=9\text{mm}$); (e) super-critical forcing ($\lambda_f=12\text{mm}$).

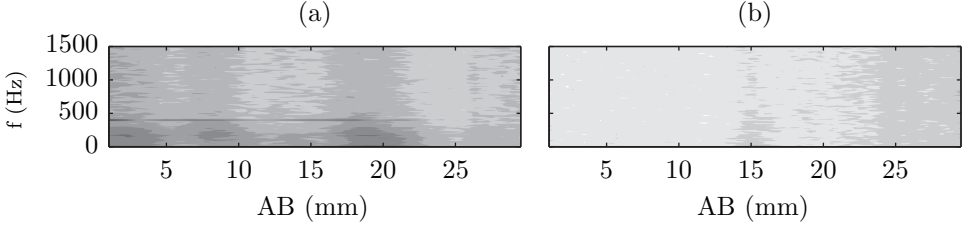


Figure 20: Same notation as figure 19 for the fields of figure 16 (10 levels, from -60 (white) to -30dB (black)). (a) $f_f=0.4\text{kHz}$ - $E=3\text{kV}$ ($C_\mu=0.013$); (b) $f_f=2\text{kHz}$ - $E=2\text{kV}$ ($C_\mu=0.037$).

nisms cannot be directly inspected in the frequency domain. This analysis is presented in the remainder, capitalising on the measurements spatial resolution.

The velocity spectra of the velocity fields of figure 16 are shown in figure 20. Forcing the flow at $f_f=0.4\text{kHz}$ - $E=3\text{kV}$ ($C_\mu=0.013$), enhances the low frequency modes considerably, as expected. A narrow band of strong fluctuations at the forced frequency is clearly distinguishable thus suggesting the receptivity of the particular flow to this range of frequencies. The fluctuations are less modulated along the span than the energy comprised in the band $0\text{Hz} \leq f \leq 350\text{Hz}$ which occur at the locations of local velocity shears in the time-averaged fields. These two bands appear rather distinguished suggesting a different origin. While the 400Hz fluctuations are directly introduced by the actuator, the lower frequency, wider-band fluctuations resemble those reported in figure 19b-e.

For the case of $f_f=2\text{kHz}$ - $E=2\text{kV}$ ($C_\mu=0.037$), the actuation introduces rather weak velocity fluctuations. The spectrum is similar to the unforced field of figure 19(a) as for this voltage the actuator has reduced strength.

7.2.3. Spatial organisation

The results discussed hitherto confirm the initial estimations towards the applicability of AC-DBD plasma actuators for control of cross-flow instabilities based on the UFD approach. More specifically, the capability of conditioning the amplified stationary mode with spanwise-modulated actuators is experimentally demonstrated for the swept wing case, analogous to the work of Schuele *et al.* (2013) in the supersonic cone case. However, the effects of forcing on the unsteady field result to strong amplification of travelling modes, which potentially can have detrimental effects for future LFC purposes.

Towards gaining insight on the low frequency fluctuations enhanced by the unsteady actuation (§ 7.2.2), description of the spatial organisation of the fluctuating velocity fields is sought. The unsteady flow field pertaining to a single stationary wave is analysed. Unsteady fluctuations are stronger when the stationary vortex is more amplified due to elevated shears. As such, the flow field encompassing the most amplified stationary vortex (CFV1, enclosed by the (red) rectangle in figures 13 and 18) is henceforth considered. Two forcing cases pertaining to the critical mode forcing ($\lambda_f=9\text{mm}$) and the spanwise-uniform forcing are selected for comparison in the following analysis. The choice of these cases is dictated by their inherently different spectrum. While the $\lambda_f=9\text{mm}$ forces the most critical stationary mode, the uniform forcing case is spanwise invariant and, as such, does not favour a certain wavelength.

Irrespective of the chosen forcing case, the velocity fluctuations occurring at this stage of the boundary layer development are still rather weak and therefore challenging to identify considering the experiment dynamic range. Technically, the latter could be increased by augmenting the PIV laser pulses separation, however such approach would compromise the effective resolution of the velocity shears (Scarano 2002). As such, statistical decomposition based on spatial coherence is employed. More specifically, proper orthogonal decomposition following the snapshot formulation (Sirovich 1987) is used, similar to previous analyses on tomo-PIV data by Serpieri & Kotsonis (2016).

As mentioned, Serpieri & Kotsonis (2016) investigated the same flow case as the one considered in the present study, albeit using DREs for conditioning the cross-flow vortices. They reported that a significant portion of kinetic energy, captured by the first POD mode, was related to a low frequency oscillation of the stationary vortices. Further analyses on less energetic POD modes allowed the identification of flow structures related to the *type-I* and *type-III* instabilities. The *type-I* mode, corresponding to a secondary instability mode of the strong spanwise shears (Högberg & Henningson 1998; Kawakami *et al.* 1999; Malik *et al.* 1999; Wassermann & Kloker 2002) was shown to be of Kelvin-Helmholtz nature (Bonfigli & Kloker 2007). Serpieri & Kotsonis (2016) reported the *type-I* mode to have a wavelength of about 4.6mm along the stationary vortices axes and occur in a range of frequencies centred at 5kHz. The *type-III* mode is instead caused by the interaction of primary stationary and travelling waves (Fischer & Dallmann 1991; Högberg & Henningson 1998; Kawakami *et al.* 1999; Malik *et al.* 1999). Serpieri & Kotsonis (2016) found these vortices to have a wavelength of 25mm and a frequency of $\approx 500\text{Hz}$.

The high sampling frequency of the current experiment allows direct investigation of the temporal evolution of the low frequency fluctuations (i.e. the *type-III* mode for the flow cases where stationary vortices have amplified). The secondary instability modes are instead occurring at higher frequencies, which lie beyond the measured band. Analysis of the temporal coefficients of the POD modes can infer the nature of the related structures. The spectra of the first 30 POD modes temporal coefficients is shown in figure 21 for the cases of spanwise-uniform forcing and critical forcing at $\lambda_f=9\text{mm}$. The spectra frequency

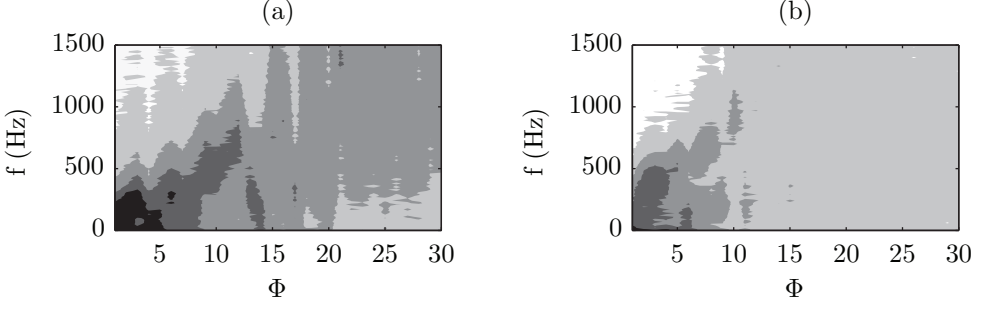


Figure 21: Power spectra ($\delta_f=10\text{Hz}$) of the first 30 POD modes' time coefficients (5 levels, from -20 (white) to 10dB (black)). The DBD plasma actuator is operated at $f_f=2\text{kHz}$ - $E=3\text{kV}$ ($C_\mu=0.046$). (a) spanwise-uniform forcing; (b) critical forcing ($\lambda_f=9\text{mm}$).

resolution is $\delta_f=10\text{Hz}$. When the spanwise-uniform actuator is employed, high energy levels are observed in the presented POD modes-frequency plane. In particular almost 50% of the total turbulent kinetic energy (TKE) pertains to the first ten POD modes (not shown). These first ten modes feature most of their energy in the $0\text{Hz} \leq f \leq 500\text{Hz}$ band, further corroborating the outcomes of figure 19(b). For the spanwise-uniform forced flow, the absence of strong stationary vortices, and related shears, leads to a different instability evolution without the growth of secondary high frequency instability modes. A continuous energy cascade towards higher frequency eddies and higher POD modes is therefore characterising the flow.

In the presence of strong stationary waves (figure 21b), the spectral energy is less spread through the POD modes. POD mode 1 shows very high energy at the lowest frequencies and is related to the POD mode 1 observed by Serpieri & Kotsonis (2016). High energy concentrations occur in the first ten POD modes, featuring strong fluctuations within the band $0\text{Hz} \leq f \leq 500\text{Hz}$ and reaching the relative cumulative TKE level of 23% (not shown). This is the frequency band where the primary travelling waves are expected as predicted by LST (§ 3), as well as experimentally observed by Serpieri & Kotsonis (2016). Proceeding towards higher index modes, the associated energy shifts towards higher frequencies beyond the resolved band. In fact, inspection of the POD eigenmodes, suggests that these POD modes pertain to *type-I* secondary instability mechanisms along the stationary vortex shears (as will be shown in § 7.2.4). These modes feature frequencies in the range of 4-9kHz for the same flow case, as reported in Serpieri & Kotsonis (2016). Due to the limited PIV sampling rate in the present study, frequencies higher than 1500Hz are not resolved. This limits the following analysis to the low frequency/high energy fluctuations.

A reduced-order reconstruction of the instantaneous velocity field based on the first 10 POD modes, which were shown to be resolved in time by the performed measurement, is presented in figure 22, for the same flow fields of figure 21. Three subsequent instantaneous flow fields, separated from each other by $\Delta_t=1/3000\text{Hz}=3.3 \cdot 10^{-4}\text{s}$, are plotted by means of U'_t velocity contours. When spanwise-uniform forcing is supplied, strong velocity fluctuations take place compared to the unforced flow field shown in figure 18a. These fluctuations are captured in the reconstructed field of figure 22a. They appear as a sequence of broad structures, spanning the entire vertical extent of the field and advected mainly along X with a smaller oscillating component along the Z direction. The reconstructed time series for the case of critical spanwise-modulated forcing ($\lambda_f=9\text{mm}$)

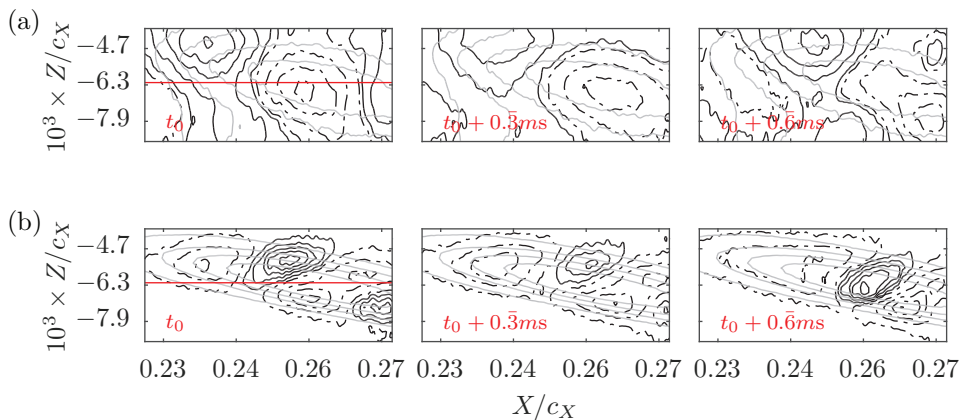


Figure 22: Reconstructed time sequence of the U'_t velocity fields (mean subtracted) from the first 10 POD modes (black lines: solid (positive) and dashed-dotted (negative), 5 levels, from ± 0.058 to $\pm 0.004U_\infty$) and time-averaged velocity field (solid grey lines: 5 levels, from 0.84 to $1U_\infty$). The flow fields presented here are shown with the (red) rectangle in figures 13 and 18 (b and d). (a) spanwise-uniform forcing; (b) critical forcing ($\lambda_f=9\text{mm}$). The solid (red) lines in the leftmost contour refer to figure 23.

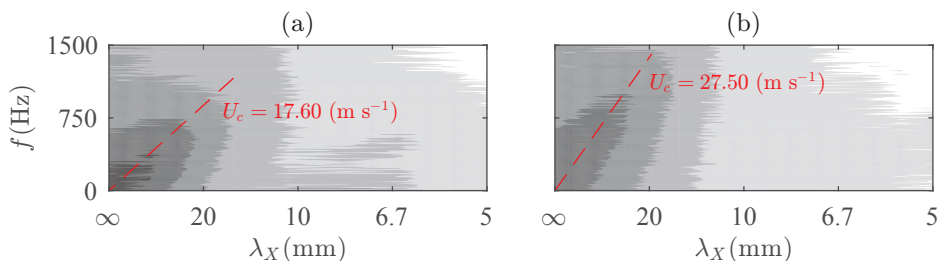


Figure 23: Wavenumber-frequency power spectra for $g = g(X, t)$ of the full time series presented in figure 22 (6 levels, from -15 (white) to 35dB (black)). (a) spanwise-uniform forcing; (b) critical forcing ($\lambda_f=9\text{mm}$). The velocity signal were extracted along the (red) solid lines shown in the leftmost contours of figure 22. The (red) dashed lines indicate the phase velocities (U_c).

is presented in figure 22b. In this case, the flow structures appear significantly smaller and localised in space compared to the spanwise-uniform forced flow. The structures are advected downstream, moving from the downwelling flow region towards the upwelling region of the stationary waves similarly to what reported in previous studies for the *type-III* modes (Högberg & Henningson 1998; Kawakami *et al.* 1999; Malik *et al.* 1999; Wassermann & Kloker 2002; Bonfigli & Kloker 2007; Serpieri & Kotsonis 2016).

The presented time sequence encompasses a total period of $\approx 1\text{ms}$ hence it is not representative of the whole fluctuations evolution. To better represent the latter, a spectral analysis is sought. The instantaneous velocity signal for the entire measurement time (2s) is sampled along a line parallel to X and centred in the domain of figure 22 (along the (red) solid line in the leftmost contours). The signals are therefore function of

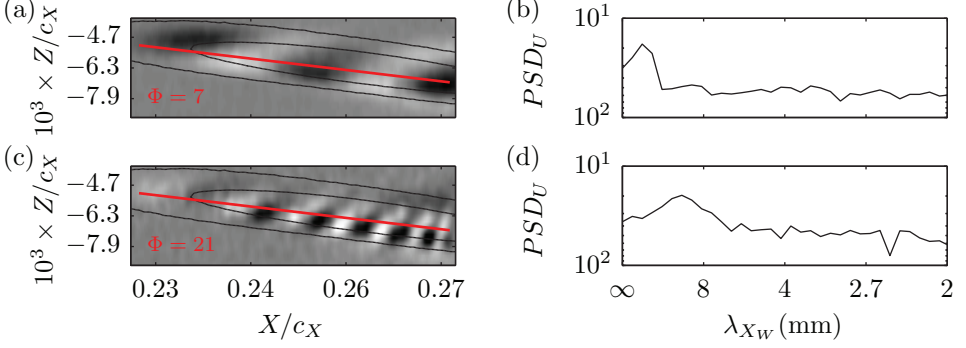


Figure 24: (a and c) U velocity fields of normalised POD modes (mode index indicated in the lower left corner) (shaded: 11 levels comprised between ± 0.05) and time-averaged velocity field (solid black lines: 3 levels, from 0.84 to $1U_\infty$). The flow fields presented here are shown with the (red) rectangle in figures 13(d) and 18(d) (critical forcing ($\lambda_f=9\text{mm}$)). (b and d) Wavenumber power spectral density of the velocity signal sampled along the (red) line, inclined along the stationary vortex of (a) and (c), respectively.

X and time: $g = g(X, t)$. The g signals are divided in segments of 600 time samples with 50% overlap between neighbouring segments, weighted with a two-dimensional Hanning function and decomposed in their spatio-temporal Fourier modes. The resulting frequency-wavenumber spectra are then averaged together (Welch 1967). The spectra have a frequency resolution of $\delta_f=10\text{Hz}$ and a spatial resolution of $\lambda_X^{min}=2.16\text{mm}$ (two times the size of the interrogation windows (Schrijer & Scarano 2008)).

The spectra are shown in figure 23 for the two considered cases. The relation between the wavenumber and the frequency, directly corresponding to the structures phase velocity (referred to as $U_c = f\lambda_X$), can be retrieved from the presented plots. A least-squares linear fit (dashed (red) lines in figure 23) through the energy maxima per wavelength was applied on the spectra giving the values of $U_c = 17.60\text{m s}^{-1}$ ($0.69U_\infty$) for the spanwise-uniform actuator and $U_c = 27.50\text{m s}^{-1}$ ($1.08U_\infty$) for the critical mode flow. The different values of advection velocity correlate with the lower values of the local velocity seen in the time-averaged fields (figure 13b and d). The phase velocity component in the Z direction could be estimated in a similar fashion (sampling the velocity time series along the Z direction). However, given the small magnitude of this velocity component, the results are not deemed reliable.

Summarising, while the instantaneous fields for the critical stationary mode case are dominated by *type-III* structures, strong velocity fluctuations mainly advecting along the free stream direction are amplified by the unsteady 2-D forcing. These observations indicate that, for the current flow cases, the unsteady flow field is strongly modified by the used plasma actuators. In section 8 a further effort in understanding this phenomenon is presented. Despite this undesired effect, the actuators showed authority in conditioning the developing CFI to the forced modes. Therefore a comparative analysis of the unsteady fields pertaining to the different forced modes can be sought.

7.2.4. UFD flow control using plasma actuators

In this section, the unsteady fields of the spanwise-modulated forcing cases are further examined within the perspective of UFD flow control. To this goal, the unsteady fields pertaining to the three forced wavelengths cases (same forcing amplitude) are reconstructed from selected POD modes. The POD modes were first analysed in their

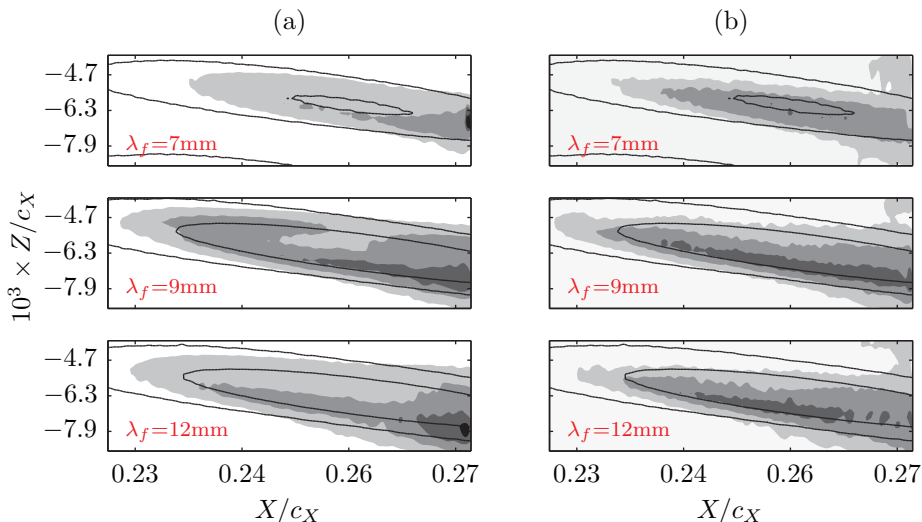


Figure 25: Standard deviation of the reconstructed U field from POD: (a) modes with $\lambda_{X_w} > 20\text{mm}$; (b) modes with $\lambda_{X_w} \leq 20\text{mm}$ (shaded: 5 levels, from 0 (white) to $0.04U_\infty$ (black)) and time-averaged velocity field (solid black lines: 3 levels, from 0.84 to $1U_\infty$). The flow fields presented here are shown with the (red) rectangle in figures 13 and 18 (c,e).

wavenumber spectral content along lines parallel to the CFVs axes (inclined -2.12° at the measurement location with respect to X). Note that, given this small angle, approximately the same wavelength limits described in the previous section are resolved. In figure 24, two POD modes with longer and shorter-wavelength structures, respectively, are shown together with the wavenumber velocity spectra along the stationary vortices to illustrate the followed procedure.

Serpieri & Kotsonis (2016) report, for the same flow field, wavelengths of $\lambda_{X_w} = 25\text{mm}$ for *type-III* modes and of $\lambda_{X_w} = 4.6\text{mm}$ for *type-I* modes. Following their results, the wavelength $\lambda_{X_w} = 20\text{mm}$ was used here as a dividing threshold to reconstruct the U fluctuations in two bands. Similarly, White & Saric (2005) and Serpieri & Kotsonis (2016) used time filters to separate the different frequency bands from hot-wire measurements. The results are presented in figure 25. It can be seen that, for both the longer and shorter-wavelengths bands, the sub-critical control mode ($\lambda_f = 7\text{mm}$) demonstrates lower fluctuations level. The other stationary modes show enhanced disturbances. This is especially evident for the shorter-wavelength disturbances, which are related to secondary mechanisms (note that these modes are not resolved in time, given the high frequency as shown in figure 21). These are located on the outer upwelling flow side of the stationary waves (Malik *et al.* 1999; Wassermann & Kloker 2002), as shown in figure 24c. This analysis further corroborates the known beneficial aspects of the UFD flow control approach on the evolution of secondary instability mechanisms.

8. Effects of plasma forcing on flow stability: a simplified model

As shown in section 7.2, the plasma actuator operation leads to strongly enhanced unsteady disturbances in the boundary layer. Two mechanisms are considered as drivers of this effect. The first pertains to the actuator's unsteady nature. It is well known

from previous plasma characterisation studies (Kotsonis 2015), as also shown in section 5.2, that the plasma actuators feature a strong periodic forcing component, associated with the AC frequency of the high-voltage input signal. Additionally, Pereira *et al.* (2015), provided an analytical model, demonstrating the strong receptivity of laminar boundary layers to high frequency forcing. Nonetheless, low frequency fluctuations were also observed in the boundary layer (figure 8). Considering these events in the context of the swept wing transition scenario, the introduced disturbances can interact with and condition the primary and secondary cross-flow instabilities. This type of interaction will be hereafter referred to as *unsteady effect*. The second considered mechanism relates to the effects of actuation on the time invariant flow. The actuator time-averaged forcing might modify the receptivity/stability characteristics of the local boundary layer, thus possibly indirectly affecting the amplification of unsteady modes (P. C. Dörr & M. J. Kloker, private communication). This mechanism is named henceforth as *steady effect*. In this section an effort is made towards verifying whether the forcing, its magnitude and direction, change the boundary layer stability. No conclusions about eventual effects on the receptivity can be retrieved from the proposed approach.

Recently, Dörr *et al.* (2017) showed effective UFD control also in the presence of OS free stream eigenmodes (with different shape, frequency and relative position with respect to the actuator) impinging on the forced boundary layer. Nevertheless, also in that study, no conclusions could be made on the forcing effect on the local boundary layer receptivity.

8.1. Model and flow cases

The suggested model is based on the addition of the actuator body-force as a source term in the stationary, incompressible laminar boundary layer equations for the case of spanwise invariant flow (2.5-D flow) presented in appendix A. Therefore, the analysis will focus on the generalised case of spanwise-uniform forcing. The inclusion of the plasma effect can be conveniently modelled as a volume distributed body-force that can be extracted with numerical or experimental means (Kotsonis 2015). It must be noted that certain assumptions are necessarily attached to such approach. It is assumed that the external flow does not affect the plasma actuator body-force (Dörr & Kloker 2015*b*, 2016; Pereira *et al.* 2014), and thermal effects due to plasma are weak enough to assume incompressible conditions (Kotsonis 2015). Additionally, the force is assumed to be time invariant (recall the definition of *steady effect* given in the previous paragraph) and of negligible magnitude in the wall-normal direction ($F_y \approx 0$). The latter is a common assumption (Dörr & Kloker 2015*a*) and is essential in the boundary layer formulation of the Navier-Stokes equations as wall normal pressure invariance ($\partial p / \partial y = 0$), upon which the system of equations A.1, A.2 and A.3 is based, will otherwise not hold (Schlichting & Gersten 2000). Finally, x diffusion terms are also neglected. The stated set of assumptions allows the modification of only the x -momentum equation as shown in equation 8.1,

$$u \frac{\partial u}{\partial x} + v \frac{\partial u}{\partial y} = -\frac{1}{\rho} \frac{\partial p}{\partial x} + \nu \frac{\partial^2 u}{\partial y^2} + \frac{F_x}{\rho} \quad (8.1)$$

The boundary layer equations A.1, 8.1, A.3 with the boundary conditions described in appendix A are integrated with the same numerical solver used for the stability analyses of section 3. The body-force field (F_x), measured in the dedicated experiment of section 5, was smoothed and interpolated at the actuator's chordwise position on the solver grid.

To investigate the effects of both forcing direction and magnitude, five cases are presently considered. Additional to the unforced baseline case, two cases consider the use of the body-force field ($C_\mu=0.046$) of figure 7*b* oriented along and against the boundary

Actuator	Forcing direction	C_μ	Case
none	-	-	unforced
2D	x	0.046	$1F_x$
2D	-x	0.046	$-1F_x$
2D	x	0.230	$5F_x$
2D	-x	0.230	$-5F_x$

Table 3: Modelled flow cases. Body-force distribution of figure 7b.

layer flow in x respectively, thus respecting the semi-infinite (spanwise invariant) swept wing assumption. Finally, two cases consider a fivefold body-force ($C_\mu=0.230$) oriented again along and against the flow in x . An overview of the modelled cases, and respective notation, is given in table 3.

8.2. Results

The boundary layer solutions for the unforced, $5F_x$ and $-5F_x$ cases, at three different chordwise stations close to the actuator, are shown in figure 26. The onefold body-force results (cases $1F_x$ and $-1F_x$) are not shown for ease of visualisation. The velocity profiles in the proximity of the actuator are inspected in the inviscid streamline system (figure 3b) as the CFI modes directly descend from the amplitude of the cross-flow component ($-w_{ISL}$).

Considering that, at the actuators location, the inviscid streamline angle is -59.73° from x , forcing along x has an enhancing effect on both the streamwise and cross-flow velocity components. The opposite holds when the induced jet is along $-x$, i.e. the actuator opposes both components as shown in figure 26. However, already at $x/c=0.1$, the forced flow profiles tend to collapse on the unforced flow curve, with differences of less than 2% (figure 26b). Considering the weak induced velocity, the body-force magnitude and spatial extent (note that the fivefold amplification affects only the body-force magnitude and not its shape) measured in section 5.2, it is expected that the actuation effects do not extend for long portions of the chord.

The flow stability of the considered five cases is analysed with LST. The analysis presented here is limited to the stationary modes and to the unsteady modes with $f=200\text{Hz}$ as this frequency features high energy at the measurement location (figure 19(b)). The related N -factor curves are presented in figure 27. The integral effect of the forcing direction can be inspected from these plots. For all the modes, the forcing along x has destabilising effects. Alternatively, forcing along $-x$, stabilises both stationary and travelling modes. The N -factors for the $1F_x$ ($-1F_x$) case lie in between the $5F_x$ ($-5F_x$) case and the unforced flow and are not shown. These results are in agreement with the outcomes of Dörr & Kloker (2015b, 2017) and are direct consequence of the mean-flow modifications shown in figure 26.

The N factor curves (figure 27) show how a rather weak and confined perturbation of the mean flow influences the flow stability characteristics, considering the integral nature of the N factors. Moreover, they show that increasing λ_z , thus driving β_r and Ψ ($\Psi = \tan^{-1}(\beta_r/\alpha_r)$) closer to zero, the CFI modes become less amplified and the forcing effect reduces. Eventually, very close to the actuator, the effect of the forcing direction inverts for waves with smaller Ψ i.e. waves travelling mainly along x (not shown). However, these waves are highly stable for most of the considered flow (given the strong favourable pressure gradient) and are far from the most amplified mode thus usually

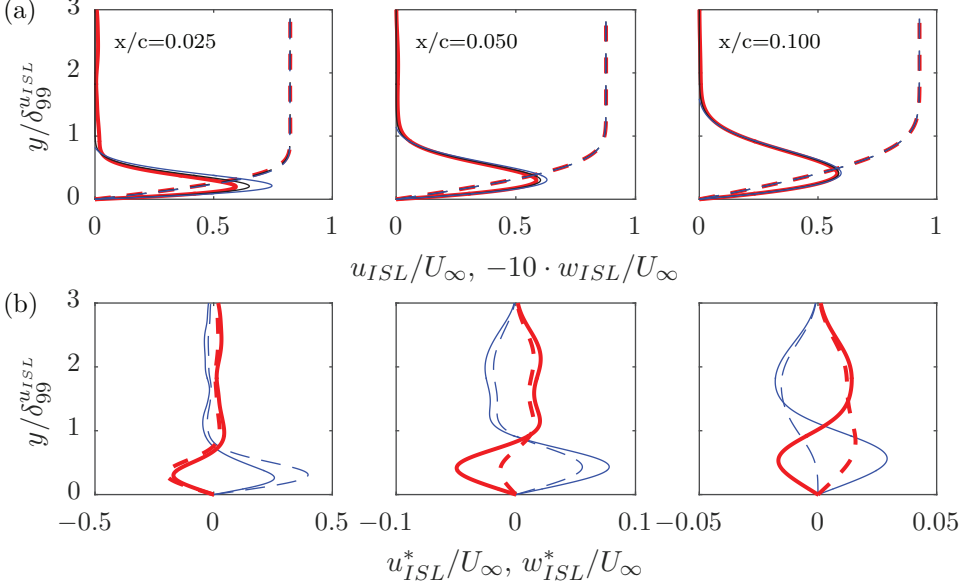


Figure 26: (a) Velocity profiles along (u_{ISL} : dashed line) and orthogonal (w_{ISL} : solid line) to the inviscid streamline at three different stations (upper left corner): unforced (black line); $5F_x$ (thin (blue) line); $-5F_x$ (thick (red) line). (b) Velocity difference profiles (u_{ISL}^* : dashed line; w_{ISL}^* : solid line) between the forced ($5F_x$: thin (blue) line); $-5F_x$: thick (red) line) and unforced case at same stations of (a). The wall normal axis is non-dimensionalised with the boundary layer thickness based on $0.99 \cdot u_{ISL}$ from the local unforced profile.

they are not observed in three dimensional boundary layers (Wassermann & Kloker 2003). The analysis presented in § 7.2.3 identified waves mainly advected along the local flow direction (roughly coinciding with X at the measurement location). From these considerations, it is concluded here that the observed enhanced low frequency fluctuations at the measurement location must be caused by the actuator *unsteady effect* attributed to a combination of low frequency fluctuations directly introduced by the actuator or to nonlinear interactions between the plasma jets and local boundary layer modes. A further detailed receptivity measurement/analysis of this effect is deemed necessary to fully elucidate this effect (see also the comments of Dörr *et al.* (2017) on this point).

Summarising, it becomes evident that the $-x$ forcing actuator has the beneficial effect of reducing the cross-flow velocity component (figure 26) thus stabilising the boundary layer with respect to stationary and travelling CFI modes (figure 27). As shown by Dörr & Kloker (2017), the forcing direction is more effective for boundary layer stabilisation when against the mean cross-flow (i.e. along z_{ISL}). However, the direction along which the actuators have the highest UFD authority is against the local flow (i.e. along $-x_{ISL}$) as it maximises the flow blockage. Therefore, a compromise between the actuator's UFD authority and CF counteraction can lead to the decision of aligning the actuator-induced jets with $-x$, thus orienting the forcing components along z_{ISL} and $-x_{ISL}$ (as shown in figure 3b). Furthermore, the combined effect of two and three-dimensional forcing, the former along z_{ISL} and the latter along $-x_{ISL}$, could sum together to some extent the two beneficial approaches (UFD and CF counteraction) for further stabilisation effects,

(a)

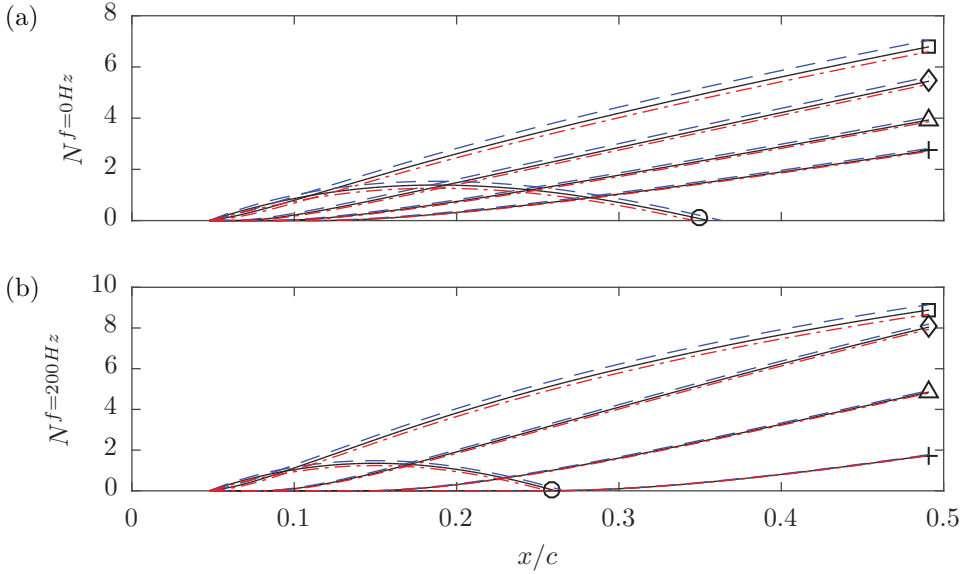


Figure 27: N-factors of different modes for $f=0\text{Hz}$ (a) and $f=200\text{Hz}$ (b) (\circ : $\lambda_z=4.5\text{mm}$; \square : $\lambda_z=9\text{mm}$; \diamond : $\lambda_z=13.5\text{mm}$; \triangle : $\lambda_z=18\text{mm}$; $+$: $\lambda_z=22.5\text{mm}$): unforced (solid black line); $5F_x$ (dashed (blue) line); $-5F_x$ (dashed-dotted (red) line).

in an analogous manner to the ‘formative suction’ control studied by Messing & Kloker (2010).

9. Discussion and concluding remarks

An experimental investigation on the effect of AC-DBD plasma actuators on cross-flow instability (CFI) modes is performed. The flow control philosophy holds on the DRE/UFD sub-critical forcing approach, where stationary modes at smaller wavelength than the naturally dominating mode are forced with leading edge devices (Saric *et al.* 1998; Malik *et al.* 1999; Wassermann & Kloker 2002). Plasma actuators could potentially provide a viable alternative to passive roughness elements due to several inherent features. Firstly, their operation is easily adjustable through remote manipulation of the electric driving signal, allowing real time adaptations of forcing amplitude and frequency (Corke *et al.* 2010). Additionally, through strategic fabrication and integration on the wing, varying spanwise wavelengths can be forced by activating or deactivating selected number of actuators. Indeed, based on novel fabrication techniques, customised and low thickness actuators can be designed specifically for cross-flow instability control. The combination of these features, makes these actuators ideal for active flow control throughout the entire flight envelope (i.e for different Reynolds numbers and wing incidences). Finally, a control strategy that holds on tuning the natural flow stability, as the UFD concept, requires only moderate input energy, assuring significant net improvement in efficiency of the control device (Dörr & Kloker 2017).

Despite these advantages, the use of AC-DBD plasma actuators for controlling CFI poses significant technical and theoretical challenges. Apart from reliability consider-

ations, which pertain more to industrial applications, their inherent unsteady forcing effect becomes highly important for flight Reynolds number flows. At these regimes, primary and secondary cross-flow instabilities appear at frequencies which are of the same order as the frequencies typically used for the plasma AC high voltage ($O(\text{kHz})$). This allows for the actuator to trigger the primary travelling CF waves or secondary cross-flow instabilities and potentially promote transition, restricting any benefits from the steady UFD effect. This possibility was already highlighted by Dörr & Kloker (2017) in their numerical simulations using plasma actuators as UFD devices. However, this effect has received limited attention up to now as the published numerical studies of Dörr & Kloker (2015*b*, 2017); Dörr *et al.* (2017) and Shahriari (2016) consider steady (or very high frequency unsteady) body-force models for the used plasma actuators. In their experimental study, Schuele *et al.* (2013), which employed UFD plasma actuators on a supersonic yawed cone experiment, did not infer the unsteady flow field. This aspect is considered crucial, as CFI-dominated boundary layers are highly receptive to fluctuations (Deyhle & Bippes 1996). Therefore, the main object of the current study was the analysis of the steady as well as unsteady mechanisms pertaining to the use of AC-DBD plasma actuators as UFD devices.

Novel actuators were therefore developed, characterised and used on a $2.17 \cdot 10^6$ Reynolds number swept wing flow. Four geometries were tested allowing to force the critical mode, a shorter-wavelength mode and a longer-wavelength mode (i.e. a sub-critical and a super-critical mode, respectively). To isolate the wavelength effect and to better analyse the consequences of using AC-DBD plasma actuators on the unsteady flow field, a spanwise-uniform actuator was tested as well. All the actuators were operated at an AC frequency ten times higher than the most unstable travelling CFI mode. A case where the actuators were operated in the unstable CFI band was also tested for comparison. Finally, a reduced-voltage test allowed to inspect the effect on the boundary layer of lowering the forcing amplitude and to compare the actuators with passive roughness elements from a previous experiment (Serpieri & Kotsonis 2016).

Infrared thermography visualisation highlighted the authority of spanwise-modulated plasma actuators in conditioning stationary CFI modes at the selected wavelengths. Quantitative boundary layer measurements were carried out using high-speed PIV. These measurements corroborated the outcomes of the flow visualisation, further indicating a reduced growth for the sub-critically forced CFI, compared to the growth of the critical modes. Consequently, also the unsteady flow field (i.e. primary and secondary instability modes) showed reduced amplitudes for the sub-critical flow case in line with the DRE/UFD studies (Saric *et al.* 1998; Wassermann & Kloker 2002; Lohse *et al.* 2016). However, spectral analysis of the unsteady velocity field showed strong enhancement of fluctuations in the actuated flow cases, irrespective of the forced wavelength. The developing flow structures were further investigated and characterised through proper orthogonal decomposition and reduced-order model reconstruction analyses.

The origin of these fluctuations was traced back to two possible, concurrent mechanisms. The first mechanism relies on the direct introduction of disturbances by the unsteady body-force component of the employed actuators (referred to as *unsteady effect*). In the investigated conditions, LST predictions indicated no amplified primary travelling waves near the forcing frequency of 2000Hz. However, in the forced cases, enhanced velocity fluctuations within a band significantly lower than the forcing frequency were detected, suggesting of these instabilities through direct introduction of low frequency fluctuations (also observed in the actuator characterization experiments) or nonlinear interactions between the actuator pulsed jets and the boundary layer modes. The second mechanism is a *steady effect*: the steady forcing component locally modifies

the mean boundary layer, and by consequence its stability and receptivity characteristics to different modes (Dörr & Kloker, private communication). As such, the boundary layer could amplify unsteady modes, originating from the *unsteady effect* of the actuators or from receptivity to free stream disturbances (Dörr *et al.* 2017).

This hypothesis was inspected through a simplified model, making use of numerical solutions of the forced boundary layer and linear stability theory. The outcomes of this investigation, as well as the *unsteady effect* require further dedicated efforts. However, through the presented model, it was possible to show that the *steady effect*, at least within the coverage of linear stability, has negligible consequences on the time-invariant flow stability. No conclusions on the effects on the boundary layer receptivity can be made at this point. Furthermore, through the actuator characterisation experiment, low frequency fluctuations were observed thus suggesting the *unsteady effect* as the cause of the enhanced low frequency fluctuations. As a consequence of these findings, UFD plasma actuators for effective LFC need to be designed, built and operated such to minimise the introduction of low frequency disturbances.

Additional to UFD configurations, plasma actuators can also be used to directly change the base flow to a more stable state. Forcing against the local cross-flow (along z_{ISL} , see figure 3b), leads to the optimum boundary layer stabilisation of CFI as it minimises the cross-flow velocity component (Dörr & Kloker 2015b). However, when the plasma forcing is against the local flow velocity (along $-x_{ISL}$), the strongest effects in inducing the monochromatic forced mode are obtained. This choice is optimal for plasma-based UFD, as it maximises the local flow blockage.

Acknowledgments

This project is funded by the Netherlands Organisation for Scientific Research *NWO-STW* under the *Veni* grant. The authors are thankful to Dr M. Kloker and P. Dörr (Institut für Aerodynamik und Gasdynamik, TU Stuttgart) for fruitful discussions. The authors acknowledge the anonymous referees for their constructive comments.

Appendix A. Laminar boundary layer solution

In this appendix, the mathematical formulation and the solver details of the laminar boundary layer solutions used in § 3 and § 8 are introduced. The 2.5-D, steady, incompressible boundary layer equations are presented in equations A.1 A.2 and A.3 (Schlichting & Gersten 2000),

$$\frac{\partial u}{\partial x} + \frac{\partial v}{\partial y} = 0 \quad (\text{A.1})$$

$$u \frac{\partial u}{\partial x} + v \frac{\partial u}{\partial y} = -\frac{1}{\rho} \frac{\partial p}{\partial x} + \nu \frac{\partial^2 u}{\partial y^2} \quad (\text{A.2})$$

$$u \frac{\partial w}{\partial x} + v \frac{\partial w}{\partial y} = \nu \frac{\partial^2 w}{\partial y^2} \quad (\text{A.3})$$

where ν is the kinematic viscosity. To be noted that, based on flow invariance along z , the z -momentum equation is decoupled from the others. This set of equations is solved on a Cartesian grid (wing curvature not accounted) stretched such to have x coinciding with the wing curvilinear abscissa. Besides the non-slip, non-penetration conditions at the wall, Dirichlet boundary conditions are prescribed at the inflow of the domain (just

after the stagnation point) with an analytical Falkner-Skan-Cooke solution at equivalent pressure gradient. At the top domain the external velocity distributions specified in A.4 are used,

$$u|_{y=\infty} = \sqrt{\mathbf{V}(x)^2 - w_\infty^2}; \quad w|_{y=\infty} = w_\infty = U_\infty \cdot \sin(\Lambda); \quad v|_{y=\infty} = 0; \quad (\text{A.4})$$

where \mathbf{V} is the velocity vector. This quantity is retrieved from the first-order linearisation of the pressure coefficient (C_p) following equation A.5,

$$|\mathbf{V}(x)| \approx U_\infty \sqrt{1 - C_p(x)} \quad (\text{A.5})$$

where the vertical bars denote vector's magnitude. The measured pressure distribution of figure 1a is averaged between the two rows of pressure taps and is used in equation A.5. C_p is based on the free stream dynamic pressure.

The differential equations are discretised with second-order finite differences in x and with spectral elements (Chebyshev collocation method, with 500 polynomials) along y . The computed boundary layer was validated against Falkner-Skan-Cooke solutions and compared to hot-wire measurements (Serpieri & Kotsonis 2016).

REFERENCES

- ARNAL, D., GASPARIAN, G. & SALINAS, H. 1998 Recent advances in theoretical methods for laminar-turbulent transition prediction. *AIAA Paper* 1998-0223 .
- BENARD, N. & MOREAU, E. 2014 Electrical and mechanical characteristics of surface ac dielectric barrier discharge plasma actuators applied to airflow control. *Experiments in Fluids* **55** (11), 1–43.
- BIPPES, H. 1999 Basic experiments on transition in three-dimensional boundary layers dominated by crossflow instability. *Progress in Aerospace Sciences* **35** (4), 363 – 412.
- BONFIGLI, G. & KLOKER, M. 2007 Secondary instability of crossflow vortices: validation of the stability theory by direct numerical simulation. *J. Fluid Mech.* **583**, 229–272.
- BRIDGES, T.J. & MORRIS, P.J. 1984 Differential eigenvalue problems in which the parameter appears nonlinearly. *Journal of Computational Physics* **55** (3), 437–460.
- CHERNYSHEV, S., KURYACHII, A., MANUILOVICH, S., RUSYANOV, D. & SKVORTSOV, V. 2013 Attenuation of cross-flow-type instability in compressible boundary layer by means of plasma actuators. *AIAA Paper* 2013-321 .
- CORKE, T. C., ENLOE, C. L. & WILKINSON, S. P 2010 Dielectric barrier discharge plasma actuators for flow control. *Annu. Rev. Fluid Mech.* **42**, 505–529.
- DEYHLE, H. & BIPPES, H. 1996 Disturbance growth in an unstable three-dimensional boundary layer and its dependence on environmental conditions. *J. Fluid Mech.* **316**, 73–113.
- DÖRR, P.C. & KLOKER, M.J. 2015a Numerical investigation of plasma-actuator force-term estimations from flow experiments. *Journal of Physics D: Applied Physics* **48** (39), 395203.
- DÖRR, P.C. & KLOKER, M.J. 2015b Stabilisation of a three-dimensional boundary layer by base-flow manipulation using plasma actuators. *Journal of Physics D: Applied Physics* **48**, 285205.
- DÖRR, P.C. & KLOKER, M.J. 2016 Transition control in a three-dimensional boundary layer by direct attenuation of nonlinear crossflow vortices using plasma actuators. *International Journal of Heat and Fluid Flow* pp. 449–465.
- DÖRR, P.C. & KLOKER, M.J. 2017 Crossflow transition control by upstream flow deformation using plasma actuators. *Journal of Applied Physics* **121** (6), 063303.
- DÖRR, P.C., KLOKER, M.J. & HANIFI, A. 2017 Effect of upstream flow deformation using plasma actuators on crossflow transition induced by unsteady vortical free-stream disturbances. *AIAA Paper* 2017-3114 .
- DOWNES, R. S. III & WHITE, E. B. 2013 Free-stream turbulence and the development of cross-flow disturbances. *J. Fluid Mech.* **735**, 347–380.

- FISCHER, T. M. & DALLMANN, U. 1991 Primary and secondary stability analysis of a three-dimensional boundary-layer flow. *Physics of Fluids A: Fluid Dynamics (1989-1993)* **3** (10), 2378–2391.
- FRIEDERICH, T. & KLOKER, M. J. 2012 Control of the secondary cross-flow instability using localized suction. *J. Fluid Mech.* **706**, 470–495.
- GRUNDMANN, S. & TROPEA, C. 2008 Active cancellation of artificially introduced tollmien-schlichting waves using plasma actuators. *Experiments in Fluids* **44** (5), 795–806.
- HAYNES, T. S. & REED, H. L. 2000 Simulation of swept-wing vortices using nonlinear parabolized stability equations. *J. Fluid Mech.* **405**, 325–349.
- HÖGBERG, M. & HENNINGSON, D. 1998 Secondary instability of cross-flow vortices in falkner-skan-cooke boundary layers. *J. Fluid Mech.* **368**, 339–357.
- HOSSEINI, S. M., TEMPELMANN, D., HANIFI, A. & HENNINGSON, D. S. 2013 Stabilization of a swept-wing boundary layer by distributed roughness elements. *J. Fluid Mech.* **718**.
- JOSLIN, R. D. 1998 Aircraft laminar flow control. *Annu. Rev. Fluid Mech.* **30** (1), 1–29.
- JUKES, T. N. & CHOI, K.-S. 2013 On the formation of streamwise vortices by plasma vortex generators. *J. Fluid Mech.* **733**, 370–393.
- KAWAKAMI, M., KOHAMA, Y. & OKUTSU, M. 1999 Stability characteristics of stationary crossflow vortices in three-dimensional boundary layer. *AIAA Paper* 1998-811 .
- KOTSONIS, M. 2015 Diagnostics for characterisation of plasma actuators. *Measurement Science and Technology* **26** (9), 092001.
- KOTSONIS, M., GHAEMI, S., VELDHUIS, L. & SCARANO, F. 2011 Measurement of the body force field of plasma actuators. *Journal of Physics D: Applied Physics* **44** (4), 045204.
- KOTSONIS, M., GIEPMAN, R., HULSHOFF, S. & VELDHUIS, L. 2013 Numerical study of the control of tollmien-schlichting waves using plasma actuators. *AIAA Journal* **51** (10), 2353–2364.
- KOTSONIS, M., SHUKLA, R. K. & PRÖBSTING, S. 2015 Control of natural tollmien-schlichting waves using dielectric barrier discharge plasma actuators. *International Journal of Flow Control* **7** (1-2), 37–54.
- KURZ, H. B. E. & KLOKER, M. J. 2014 Receptivity of a swept-wing boundary layer to micron-sized discrete roughness elements. *J. Fluid Mech.* **755**, 62–82.
- LOHSE, J., BARTH, H. P. & NITSCHKE, W. 2016 Active control of crossflow-induced transition by means of in-line pneumatic actuator orifices. *Experiments in Fluids* **57** (8), 1–10.
- MACK, L. M. 1984 Boundary-layer linear stability theory. *AGARD Report* 709 .
- MALIK, M. R., LI, F., CHOUDHARI, M. & CHANG, C.-L. 1999 Secondary instability of crossflow vortices and swept-wing boundary-layer transition. *J. Fluid Mech.* **399**, 85–115.
- MESSING, R. & KLOKER, M. J. 2010 Investigation of suction for laminar flow control of three-dimensional boundary layers. *J. Fluid Mech.* **658**, 117–147.
- PEREIRA, R., KOTSONIS, M., DE OLIVEIRA, G. & RAGNI, D. 2015 Analysis of local frequency response of flow to actuation: Application to the dielectric barrier discharge plasma actuator. *Journal of Applied Physics* **118** (15).
- PEREIRA, R., RAGNI, D. & KOTSONIS, M. 2014 Effect of external flow velocity on momentum transfer of dielectric barrier discharge plasma actuators. *Journal of Applied Physics* **116** (10).
- RADEZTSKY, R. H., REIBERT, M. S. & SARIC, W. S. 1999 Effect of isolated micron-sized roughness on transition in swept-wing flows. *AIAA Journal* **37** (11), 1370–1377.
- RAFFEL, MARKUS, WILLERT, CHRISTIAN E, WERELEY, STEVE T & KOMPENHANS, JÜRGEN 2007 *Particle Image Velocimetry*. Springer.
- REIBERT, M. S., SARIC, W. S., CARRILLO, R. B. JR. & CHAPMAN, K. 1996 Experiments in nonlinear saturation of stationary crossflow vortices in a swept-wing boundary layer. *AIAA Paper* 1996-0184 .
- SARIC, W., REED H. & BANKS, D. 2004 Flight testing of laminar flow control in high-speed boundary layers. NATO-RTO-MP-AVT-111.
- SARIC, W., CARRILLO R., JR. & REIBERT, M. 1998 Leading-edge roughness as a transition control mechanism. *AIAA Paper* 1998-781 .
- SARIC, W. & REED, H. 2002 Supersonic laminar flow control on swept wings using distributed roughness. *AIAA Paper* 2002-147 .
- SARIC, W. S., CARPENTER, A. L. & REED, H. L. 2011 Passive control of transition in three-

- dimensional boundary layers, with emphasis on discrete roughness elements. *Philosophical Transactions of the Royal Society of London A: Mathematical, Physical and Engineering Sciences* **369** (1940), 1352–1364.
- SARIC, W. S., REED, H. L. & WHITE, E. B. 2003 Stability and transition of three-dimensional boundary layers. *Annu. Rev. Fluid Mech.* **35** (1), 413–440.
- SCARANO, F. 2002 Iterative image deformation methods in piv. *Measurement Science and Technology* **13** (1), R1.
- SCHLICHTING, H. & GERSTEN, K. 2000 *Boundary layer theory*. Cambridge University Press.
- SCHRIJER, FFJ & SCARANO, F. 2008 Effect of predictor–corrector filtering on the stability and spatial resolution of iterative piv interrogation. *Experiments in Fluids* **45** (5), 927–941.
- SCHUELE, C. Y., CORKE, T. C. & MATLIS, E. 2013 Control of stationary cross-flow modes in a mach 3.5 boundary layer using patterned passive and active roughness. *J. Fluid Mech.* **718**, 5–38.
- SERPIERI, J. & KOTSONIS, M. 2016 Three-dimensional organisation of primary and secondary crossflow instability. *J. Fluid Mech.* **799**, 200–245.
- SERPIERI, J. & KOTSONIS, M. 2017 Conditioning of unsteady cross-flow instability modes using ac-dbd plasma actuators. Under review on: *Experimental Thermal and Fluid Science* .
- SERPIERI, J., YADALA VENKATA, S. & KOTSONIS, M. 2017 Towards laminar flow control on swept wings with ac-dbd plasma actuators as active roughness. *AIAA Paper* 2017-1459 .
- SHAHRIARI, N. 2016 *On stability and receptivity of boundary-layer flows*. PhD Thesis, KTH Royal Institute of Technology, Stockholm, Sweden.
- SIROVICH, L. 1987 Turbulence and the dynamics of coherent structures. part i: Coherent structures. *Quarterly of applied mathematics* **45** (3), 561–571.
- TUCKER, A. A., SARIC, W. S. & REED, H. L. 2014 Laminar flow control flight experiment design and execution. *AIAA Paper* 2014-909 .
- WASSERMANN, P. & KLOKER, M. 2002 Mechanisms and passive control of crossflow-vortex-induced transition in a three-dimensional boundary layer. *J. Fluid Mech.* **456**, 49–84.
- WASSERMANN, P. & KLOKER, M. 2003 Transition mechanisms induced by travelling crossflow vortices in a three-dimensional boundary layer. *J. Fluid Mech.* **483**, 67–89.
- WELCH, P. D. 1967 The use of fast fourier transform for the estimation of power spectra: A method based on time averaging over short, modified periodograms. *Audio and Electroacoustics, IEEE Transactions on* **15** (2), 70–73.
- WHITE, E. & SARIC, W. 2000 Application of variable leading-edge roughness for transition control on swept wings. *AIAA Paper* 2000-283 .
- WHITE, E. B. & SARIC, W. S. 2005 Secondary instability of crossflow vortices. *J. Fluid Mech.* **525**, 275–308.